Available online at www.sciencedirect.com
SCIENCE DIRECT®
ELSEVIER
International Journal of Solids and Structures 42 (2005) 6475–6513
INTERNATIONAL JOURNAL OF SOLIDS and STRUCTURES
www.elsevier.com/locate/ijsolstr

The helicoidal modeling in computational finite elasticity. Part III: Finite element approximation for non-polar media

T. Merlini *, M. Morandini [1]

Dipartimento di Ingegneria Aerospaziale, Politecnico di Milano, Via La Masa 34, I-20158 Milano, Italy

Received 29 July 2004; received in revised form 8 June 2005
Available online 18 August 2005

Abstract

The helicoidal modeling of the continuum, as proposed in Part I, is applied to finite elasticity analyses of simple materials unable of couple-stressing. First, the non-polar medium is introduced via a constitutive postulate and results in a sort of constrained medium, having the axial vector of the Biot stress tensor as a primary unknown field and the statement of polar decomposition of the deformation gradient as a governing equation. Next, the variational formulation is accommodated to the non-polar case, and the ensuing principle is approximated by the finite element method. The nonlinear finite elements have the nodal oriento-positions as degrees-of-freedom and are based on the multiplicative interpolation developed in Part II. The interpolation and an analysis methodology based on the multiplicative updating of the kinematical unknowns, ensure frame-invariant and path-independent solutions. Several examples, with either linear or nearly incompressible Neo-Hookean elastic materials, attest the performance of the proposed modeling in high deformation problems with large three-dimensional rototranslations.

Keywords: Finite elasticity; Variational formulations; Finite rotations and rototranslations; Dual algebra; Nonlinear finite elements

1. Introduction

In Part I of the present work (Merlini and Morandini, 2004c), we developed a new concept of continuum modeling based on the relative rototranslations between any two material particles. This concept differs

* Corresponding author. Tel.: +39 02 2399 8352; fax: +39 02 2399 8334.
E-mail addresses: teodoro.merlini@polimi.it (T. Merlini), marco.morandini@polimi.it (M. Morandini).
[1] Tel.: +39 02 2399 8362; fax: +39 02 2399 8334.

0020-7683/$ - see front matter © 2005 Elsevier Ltd. All rights reserved.
doi:10.1016/j.ijsolstr.2005.06.031

from the classical modeling defined in a Euclidean space and based on the relative particle positions. The particle orientations contribute to define the path between two particles both in the sense of the material lines describing the current geometry in a given body configuration, and the particle trajectories describing the evolution along the deformation history. The rototranslation between the oriento-positions of two material particles is shown to belong to the proper orthogonal class of a special kind of tensor, namely dual tensors (tensors made of dual numbers as scalar components and obeying the algebraic rules of dual numbers, see e.g. Angeles, 1998). The tangent space of rototranslations is quite different from the tangent space of displacements, proper of the Euclidean standpoint, and is characterized by a dual vector referred to as the differential helix of the rototranslation, whence the name of *helicoidal modeling*. In Part II (Merlini and Morandini, 2004d), we established how to properly obtain a substitute field of oriento-positions within a region of continuum from a discrete set of oriento-positions. The ensuing nonlinear interpolation opens the way to a consistent finite-element approximation of the helicoidal modeling suitable for numerical analyses in large deformation problems.

The variational formulation in finite hyperelasticity, tailored to the helicoidal modeling, was presented in Part I for the general case of a polar medium, i.e. a medium capable of withstanding angular strains by opposing couple-stresses. The main variational principles in elastostatics have been derived and consistently linearized. In the present Part III, it will be shown how a simple material, unable of couple-stressing against angular strains, can be constitutively characterized as a particular case of polar medium (hence, it will be referred to as non-polar medium). A sort of constrained medium ensues, having the axial vector of the Biot stress tensor (from here on referred to as the *Biot-axial*) as a primary unknown field to be retained beside the kinematical unknown field of the helix that controls the oriento-positions within the continuum. When couple-stresses are absent, the orientation of a material particle reduces to an abstract concept, and in the present formulation it turns out to be defined by a kinematical constraint that matches the polar decomposition theorem of the deformation gradient. This constraint appears in a natural, constitutive way and arises as a governing equation beside the generalized momentum balance. Once the variational principles and their linearization have been fitted to the non-polar case, the minimal principle, having the oriento-position and Biot-axial fields as unknowns, is approximated by the finite element method.

The formulation of nonlinear finite elements in the context of the helicoidal modeling is somewhat particular. An important issue is the resolution of the mixed variation variables (denoted by two indexes $\partial\delta$, see Part II) for the virtual and incremental variables (δ and ∂) separately. This resolution cannot be carried out locally at an integration point because of the nonlinear dependency of the field variables from the discrete, global variables, but must be done at the nodal level, where the true model unknowns exist. Another issue concerns the methodology of analysis, which relies on the multiplicative updating of the nodal unknowns and on the direct interpolation of the oriento-positions and curvatures at any given configuration; the subsequent evaluation of a properly defined kinematical strain measure ensures path-independent solutions. Finally, another issue is strictly related to the non-polar constitutive model, which includes the Biot-axial constraint field as a primary unknown. Which interpolation scheme is appropriate for this field is the main concern, and the answer must conform to the genuine role of the Biot-axial of controlling the change of orientation.

The paper contains the theoretical formulation and selected numerical examples. The notation employed is provided in Section 2, then Section 3 is devoted to the constitutive characterization and variational formulation of the non-polar medium. In Section 4, the finite element approximation is formulated and the analysis methodology is discussed. The interpolation of the Biot-axial field and the main features of the proposed elements (for both three-dimensional and planar models) are detailed in Section 5. Examples of large deformation problems are given in Section 6 for linear elastic materials, and in Section 7 for nearly incompressible Neo-Hookean materials. What a 'linear' problem under the helicoidal modeling means is addressed in Section 8, and conclusions are drawn in Section 9.

2. Useful notation from Part I

The definitions of operators and quantities useful to understand the developments of Section 3 are repeated here from Part I. For the reader's convenience, they are arranged in the following list mostly in the same order in which they were introduced.

Base vectors and common operators

$\boldsymbol{i}_j \equiv \boldsymbol{i}^j$ the self-reciprocal absolute reference triad ($j = 1,2,3$)
$\boldsymbol{g}_j$, $\boldsymbol{g}^j$ the reciprocal triads of covariant and contravariant base vectors ($j = 1,2,3$)
$(\,)\times$ the vector-cross operator, providing a skew-symmetric tensor
$(\,)^\times = (\,)_j \times \otimes \boldsymbol{g}^j$, the tensor-cross operator, providing a third-order tensor
$\boldsymbol{I}^\times = \boldsymbol{g}^j \times \otimes \boldsymbol{g}_j$, the Ricci's third-order tensor
$(\,)_{/\otimes} = (\,)_{,j} \otimes \boldsymbol{g}^j$, the gradient operator
$(\,)_{/\bullet} = (\,)_{,j} \cdot \boldsymbol{g}^j$, the divergence operator
ε the dual unity, such that $\varepsilon \neq 0$ and $\varepsilon^2 = \varepsilon^3 = \cdots = 0$
primal( ) the primal part of a dual argument
dual( ) the dual part of a dual argument
$(\,)'$ refers to quantities in the current configuration
δ, ∂, $\partial\delta$ refer to virtual, incremental and mixed virtual–incremental variations, respectively

Kinematical variables

$\boldsymbol{x}$, $\boldsymbol{\alpha}$ the position vector and the orientation (orthogonal) tensor of a material particle
$\boldsymbol{X} = \boldsymbol{I} + \varepsilon\, \boldsymbol{x}\times$, the position dual tensor (the arm operator)
$\boldsymbol{A} = \boldsymbol{X}\boldsymbol{\alpha} = \boldsymbol{\alpha} + \varepsilon \boldsymbol{x} \times \boldsymbol{\alpha}$, the oriento-position dual tensor
$\boldsymbol{k} = \boldsymbol{k}_\mathrm{a} + \varepsilon \boldsymbol{k}_\mathrm{l} = \boldsymbol{A}\,\mathrm{ax}(\boldsymbol{A}^\mathrm{T}\boldsymbol{A}_{/\otimes})$, the curvature dual tensor
$\boldsymbol{k}_\mathrm{a} = \boldsymbol{\alpha}\,\mathrm{ax}(\boldsymbol{\alpha}^\mathrm{T}\boldsymbol{\alpha}_{/\otimes})$, the angular curvature tensor
$\boldsymbol{F} = \boldsymbol{x}'_{/\otimes} = \mathrm{dual}(\boldsymbol{X}'^\mathrm{T}\boldsymbol{k}')$, the deformation gradient
$\boldsymbol{H} = \boldsymbol{X}'\boldsymbol{\Phi}\boldsymbol{X}^\mathrm{T}$, the rototranslation dual tensor such that $\boldsymbol{A}' = \boldsymbol{H}\boldsymbol{A}$
$\boldsymbol{\Phi}$ the rotation tensor such that $\boldsymbol{\alpha}' = \boldsymbol{\Phi}\boldsymbol{\alpha}$
$\boldsymbol{\omega} = \boldsymbol{\omega}_\mathrm{a} + \varepsilon\boldsymbol{\omega}_\mathrm{l} = \boldsymbol{H}\,\mathrm{ax}(\boldsymbol{H}^\mathrm{T}\boldsymbol{H}_{/\otimes}) = \boldsymbol{k}' - \boldsymbol{H}\boldsymbol{k}$, the kinematical strain dual tensor
$\boldsymbol{\omega}_\mathrm{a} = \boldsymbol{\Phi}\,\mathrm{ax}(\boldsymbol{\Phi}^\mathrm{T}\boldsymbol{\Phi}_{/\otimes}) = \boldsymbol{k}'_\mathrm{a} - \boldsymbol{\Phi}\boldsymbol{k}_\mathrm{a}$, the kinematical angular strain tensor
$\boldsymbol{\chi} = \boldsymbol{F} - \boldsymbol{\Phi}\boldsymbol{I} = \mathrm{dual}(\boldsymbol{X}'^\mathrm{T}\boldsymbol{\omega})$, the kinematical 'linear' strain tensor

Loads and stresses

$\boldsymbol{f}$, $\boldsymbol{c}$ the body force and couple densities per unit initial volume
$\boldsymbol{b} = \boldsymbol{X}'(\boldsymbol{f} + \varepsilon\boldsymbol{c})$, the pole-based body load density per unit initial volume
$\boldsymbol{t}$, $\boldsymbol{m}$ the boundary force and couple densities per unit initial surface
$\boldsymbol{s} = \boldsymbol{X}'(\boldsymbol{t} + \varepsilon\boldsymbol{m})$, the pole-based boundary load density per unit initial surface
$\tilde{\boldsymbol{T}}$, $\tilde{\boldsymbol{M}}$ the stress and couple-stress tensors, analogs of the first Piola–Kirchhoff stress
$\tilde{\boldsymbol{S}} = \boldsymbol{X}'(\tilde{\boldsymbol{T}} + \varepsilon\tilde{\boldsymbol{M}})$, the pole-based first Piola–Kirchhoff dual stress tensor

Elasticity

$w(\boldsymbol{\xi})$, $v(\hat{\boldsymbol{S}})$ the strain-energy and the complementary-energy density functions
$\boldsymbol{\beta}$ the distortion strain parameter, related to the kinematical angular strain by $\boldsymbol{\beta} = \boldsymbol{\Phi}^\mathrm{T}\boldsymbol{\omega}_\mathrm{a}$
$\boldsymbol{\varepsilon}$ the stretch strain parameter, related to the kinematical linear strain by $\boldsymbol{\varepsilon} = \boldsymbol{\Phi}^\mathrm{T}\boldsymbol{\chi}$
$\boldsymbol{\xi} = \boldsymbol{\beta} + \varepsilon\boldsymbol{\varepsilon}$ the dual strain parameter, related to the kinematical strain by the compatibility condition $\boldsymbol{\xi} = \boldsymbol{X}^\mathrm{T}\boldsymbol{H}^\mathrm{T}\boldsymbol{\omega} = \boldsymbol{\Phi}^\mathrm{T}\boldsymbol{X}'^\mathrm{T}\boldsymbol{\omega}$; also defined by the inverse constitutive equation $\boldsymbol{\xi}(\hat{\boldsymbol{S}}) = v_{/\hat{\boldsymbol{S}}}$

$\hat{\boldsymbol{S}} = \hat{\boldsymbol{T}} + \varepsilon\hat{\boldsymbol{M}}$ the dual stress parameter, defined by the constitutive equation $\hat{\boldsymbol{S}}(\boldsymbol{\xi}) = w_{/\boldsymbol{\xi}}$ and related to the first Piola–Kirchhoff dual stress tensor by $\hat{\boldsymbol{S}} = \boldsymbol{X}^{\mathrm{T}}\boldsymbol{H}^{\mathrm{T}}\tilde{\boldsymbol{S}} = \boldsymbol{\Phi}^{\mathrm{T}}\boldsymbol{X}'^{\mathrm{T}}\tilde{\boldsymbol{S}}$

$\mathbb{E}$ the elastic tensor $\mathbb{E}(\boldsymbol{\xi}) = \hat{\boldsymbol{S}}_{/\boldsymbol{\xi}} = w_{/\boldsymbol{\xi}\boldsymbol{\xi}}$

3. Variational formulation of the non-polar medium

Most of the materials we commonly deal with in structural engineering do not show the constitutive behavior of a polar medium, in the sense that they are unable of couple-stressing against the particle distortion. Nevertheless, the non-polar medium can be classified as a particular case of the more general polar one. Thus, the variational formulation presented in Part I for a polar medium is also suitable for a standard simple material, provided the latter be defined by appropriately restricting the dependency of the strain energy on the strain parameter. A constitutive postulate of this kind was first proposed in our past formulation equipped with independent rotations in the context of classical modeling (Merlini, 1997). That formulation departed from the common standpoint by which the rotation is introduced via the polar decomposition theorem of the deformation gradient like an appended constraint equation. Variational formulations assuming independent rotations were pioneered by Reissner (1965), who suggested to relax the angular momentum balance into a weak condition. Nonlinear formulations were then developed by Fraeijs de Veubeke (1972) and later by Atluri (1984), Reissner (1984) and Bufler (1985); see also Atluri and Cazzani (1995) and Wisniewski (1998). Regularized principles for linear elasticity with an independent rotation field were first proposed by Hughes and Brezzi (1989) to ensure stability of the numerical approximations by finite elements based on convenient interpolations, then they were extended to finite elasticity by Simo et al. (1992), Ibrahimbegović and Frey (1995), Seki and Atluri (1994, 1995). In our approach, the constitutive characterization of a hyperelastic medium unable of couple-stressing comes in two steps, with the definition of an intermediate, so-called pseudo-polar medium. As a final outcome, the strain energy becomes dependent on a symmetric strain-parameter tensor (six scalars) and the remaining workless stress vector field (the axial vector of the Biot stress tensor) has to be retained as a primary unknown. The rank of the constitutive equation reduces, and, correspondingly, part of the compatibility condition degenerates into a mere kinematical constraint, which is seen to identify the change of particle orientation with the rotation of the medium, as defined by the polar decomposition of the deformation gradient. We thus arrive at the same constraint equation, but through a consistent deduction within a constitutive framework.

3.1. Constitutive characterization

The constitutive characterization of the hyperelastic non-polar medium is accomplished in two steps. In the first step the couple-stress is made to vanish. This is achieved by restricting the dependency of the strain-energy function: $w(\boldsymbol{\xi})$ is assumed to be independent of the angular part of the dual strain parameter $\boldsymbol{\xi}$, namely the distortion $\boldsymbol{\beta}$. In fact, by this assumption, and by writing the variation $\mathrm{d}w = \langle \mathrm{d}\boldsymbol{\xi}, w_{/\boldsymbol{\xi}} \rangle$ of the strain energy in the light of Eq. (55) of Part I, it follows that the dual stress parameter $w_{/\boldsymbol{\xi}}$ consists only of the linear part. With reference to the explicit notation introduced since Eqs. (58), Part I, the *constitutive postulate* of the strain energy w being a function of just the stretch $\boldsymbol{\varepsilon}$ as a strain parameter, can formally be stated as

$$w = w(\cancel{\boldsymbol{\beta}}, \boldsymbol{\varepsilon}) = w(\boldsymbol{\varepsilon}) \Rightarrow \begin{cases} \hat{\boldsymbol{M}} = w_{/\boldsymbol{\beta}} \equiv \boldsymbol{0}, \quad \boldsymbol{\beta} \equiv \boldsymbol{\Phi}^{\mathrm{T}}\boldsymbol{\omega}_{\mathrm{a}} \neq \boldsymbol{0}, \\ \hat{\boldsymbol{T}} = w_{/\boldsymbol{\varepsilon}} = \hat{\boldsymbol{T}}(\boldsymbol{\varepsilon}). \end{cases} \tag{1}$$

The angular part $\hat{\boldsymbol{M}}$ of the dual stress parameter $\hat{\boldsymbol{S}} = \hat{\boldsymbol{T}} + \varepsilon\hat{\boldsymbol{M}}$ becomes elastically undefined and vanishes, and so do any couple-stresses $\tilde{\boldsymbol{M}} = \boldsymbol{\Phi}\hat{\boldsymbol{M}}$. Notice, however, that a non-null distortion $\boldsymbol{\beta}$ is allowed for as a workless, purely kinematical strain field. The stress parameter reduces to the linear Biot stress tensor $\hat{\boldsymbol{T}}$, with $\hat{\boldsymbol{T}}(\boldsymbol{\varepsilon}) = w_{/\boldsymbol{\varepsilon}}$ as the constitutive equation.

The result of this first step is a medium referred to as a *pseudo-polar* medium (Merlini, 1997). It has been used in micropolar elasticity due to the far simpler elastic characterization in comparison with the polar medium (see for instance Eringen, 1966; Felippa, 1992; Yeh and Chen, 1993). The pole-based balance equations (54) of Part I in their essential dual form are still valid, with the pole-based first Piola–Kirchhoff dual stress tensor $\tilde{\boldsymbol{S}}$ (see Eqs. (53) in Part I) now expressed as $\tilde{\boldsymbol{S}} = \boldsymbol{X}'\tilde{\boldsymbol{T}} = \boldsymbol{X}'\boldsymbol{\Phi}\hat{\boldsymbol{T}} = \boldsymbol{H}\boldsymbol{X}\hat{\boldsymbol{T}}$. However, the angular balance of the self-based version (i.e. the well-known equations $\tilde{\boldsymbol{M}}_{/\bullet} + 2\mathrm{ax}(\tilde{\boldsymbol{T}}\boldsymbol{F}^{\mathrm{T}}) + \boldsymbol{c} = \boldsymbol{0}$ within the body and $\tilde{\boldsymbol{M}}\boldsymbol{v} = \boldsymbol{m}$ on the surface) reduces to the algebraic equation $2\mathrm{ax}(\tilde{\boldsymbol{T}}\boldsymbol{F}^{\mathrm{T}}) + \boldsymbol{c} = \boldsymbol{0}$ (which allows for non-symmetry of the analog of the Cauchy stress tensor $|\boldsymbol{F}|^{-1}\tilde{\boldsymbol{T}}\boldsymbol{F}^{\mathrm{T}}$ in the presence of an external couple $\boldsymbol{c}$) and to the trivial boundary condition $\boldsymbol{m} = \boldsymbol{0}$, stating that no surface couples are locally allowed. Since the workless distortion is now identically defined as $\boldsymbol{\beta} \equiv \boldsymbol{\Phi}^{\mathrm{T}}\boldsymbol{\omega}_{\mathrm{a}}$, the internal compatibility condition (Eq. (62) of Part I) reduces to the linear part alone $\boldsymbol{\varepsilon} = \mathrm{dual}(\boldsymbol{X}^{\mathrm{T}}\boldsymbol{H}^{\mathrm{T}}\boldsymbol{\omega})$, where, from now on, we denote by primal( ) and dual( ) the functions extracting the single parts from a dual argument.

Before addressing the second step of the constitutive characterization, it is useful to introduce the complementary-energy function $v(\hat{\boldsymbol{T}})$ of the pseudo-polar medium by means of the Legendre transform $v = \langle\hat{\boldsymbol{T}}, \boldsymbol{\varepsilon}\rangle - w$, having inverted the constitutive equation $\hat{\boldsymbol{T}}(\boldsymbol{\varepsilon})$ for $\boldsymbol{\varepsilon}(\hat{\boldsymbol{T}})$. Furthermore, we introduce the Euclidean decomposition of the strain and stress parameters, $\boldsymbol{\varepsilon} = \boldsymbol{\varepsilon}^{\mathrm{S}} + (\mathrm{ax}\,\boldsymbol{\varepsilon})\times$ and $\hat{\boldsymbol{T}} = \hat{\boldsymbol{T}}^{\mathrm{S}} + \hat{\boldsymbol{\tau}}\times$, where $\hat{\boldsymbol{\tau}}$ denotes the axial vector of the Biot stress and $(\,)^{\mathrm{S}}$ is a notation for the symmetric part of a tensor.

In the second step, the (linear) working parameters become symmetric tensors and the strain energy becomes a function of only *six* scalars, in agreement with the usual assumptions in classical elasticity, either based on the Biot strain or on the Green strain. This is achieved in analogy with the first step, but working now on the dependency of the complementary energy: $v(\hat{\boldsymbol{T}})$ is assumed to be independent of the skew-symmetric part of the stress parameter. Since the symmetric and skew-symmetric parts of two tensors are uncoupled in a scalar product, such as for the variation $\mathrm{d}v = \langle\mathrm{d}\hat{\boldsymbol{T}}, v_{/\hat{\boldsymbol{T}}}\rangle$ of the complementary energy, this assumption entails the symmetry of the strain parameter $v_{/\hat{\boldsymbol{T}}}$. Again, the fact that the complementary energy v is a function of only the symmetric tensor $\hat{\boldsymbol{T}}^{\mathrm{S}}$ as a stress parameter, is a *constitutive postulate*, formally

$$v = v(\hat{\boldsymbol{T}}^{\mathrm{S}}, \cancel{\times}) = v(\hat{\boldsymbol{T}}^{\mathrm{S}}) \Rightarrow \begin{cases} \boldsymbol{\varepsilon}^{\mathrm{S}} = v_{/\hat{\boldsymbol{T}}^{\mathrm{S}}} = \boldsymbol{\varepsilon}^{\mathrm{S}}(\hat{\boldsymbol{T}}^{\mathrm{S}}), \\ 2\mathrm{ax}\,\boldsymbol{\varepsilon} = v_{/\hat{\boldsymbol{\tau}}} \equiv \boldsymbol{0}, \quad \hat{\boldsymbol{\tau}} \neq \boldsymbol{0}. \end{cases} \tag{2}$$

Notice that the axial vector of the strain $\boldsymbol{\varepsilon}$ becomes elastically undefined and vanishes, while a non-null Biot-axial $\hat{\boldsymbol{\tau}}$ is allowed for as a workless stress field. The strain parameter reduces to the symmetric stretch tensor $\boldsymbol{\varepsilon}^{\mathrm{S}}$, with $\boldsymbol{\varepsilon}^{\mathrm{S}}(\hat{\boldsymbol{T}}^{\mathrm{S}}) = v_{/\hat{\boldsymbol{T}}^{\mathrm{S}}}$ the inverse constitutive equation.

To complete the characterization of the *non-polar* medium, the strain-energy function $w(\boldsymbol{\varepsilon}^{\mathrm{S}})$ is recovered by means of the Legendre transform $w = \langle\boldsymbol{\varepsilon}^{\mathrm{S}}, \hat{\boldsymbol{T}}^{\mathrm{S}}\rangle - v$, having inverted $\boldsymbol{\varepsilon}^{\mathrm{S}}(\hat{\boldsymbol{T}}^{\mathrm{S}})$ for $\hat{\boldsymbol{T}}^{\mathrm{S}}(\boldsymbol{\varepsilon}^{\mathrm{S}})$. The (direct) *constitutive equation* is then written as

$$\hat{\boldsymbol{T}}^{\mathrm{S}} = w_{/\boldsymbol{\varepsilon}^{\mathrm{S}}}. \tag{3}$$

Linearization of the stress-parameter function $\hat{\boldsymbol{T}}^{\mathrm{S}}(\boldsymbol{\varepsilon}^{\mathrm{S}})$ gives $\partial\hat{\boldsymbol{T}}^{\mathrm{S}} = \mathbb{E}_{\boldsymbol{\varepsilon}^{\mathrm{S}}\boldsymbol{\varepsilon}^{\mathrm{S}}} : \partial\boldsymbol{\varepsilon}^{\mathrm{S}}$, with $\mathbb{E}_{\boldsymbol{\varepsilon}^{\mathrm{S}}\boldsymbol{\varepsilon}^{\mathrm{S}}}(\boldsymbol{\varepsilon}^{\mathrm{S}}) = \hat{\boldsymbol{T}}^{\mathrm{S}}_{/\boldsymbol{\varepsilon}^{\mathrm{S}}} = w_{/\boldsymbol{\varepsilon}^{\mathrm{S}}\boldsymbol{\varepsilon}^{\mathrm{S}}}$ the elastic tensor, a fourth-order, three times symmetric and invertible tensor mapping $\partial\boldsymbol{\varepsilon}^{\mathrm{S}}$ on $\partial\hat{\boldsymbol{T}}^{\mathrm{S}}$.

A synopsis of the foregoing formulation is given in Box 1. This kind of constitutive characterization of the non-polar medium is also found in Merlini (1997), while two variants retaining a certain part of the couple-stress as a workless parameter were investigated in Merlini and Morandini (2002). In the present formulation, the pole-based balance equations are still Eqs. (54) of Part I, where, as for the pseudo-polar medium, $\tilde{\boldsymbol{S}}$ is lacking of the couple-stress $\tilde{\boldsymbol{M}}$, so $\tilde{\boldsymbol{S}} = \boldsymbol{X}'\tilde{\boldsymbol{T}} = \boldsymbol{H}\boldsymbol{X}\hat{\boldsymbol{T}}$:

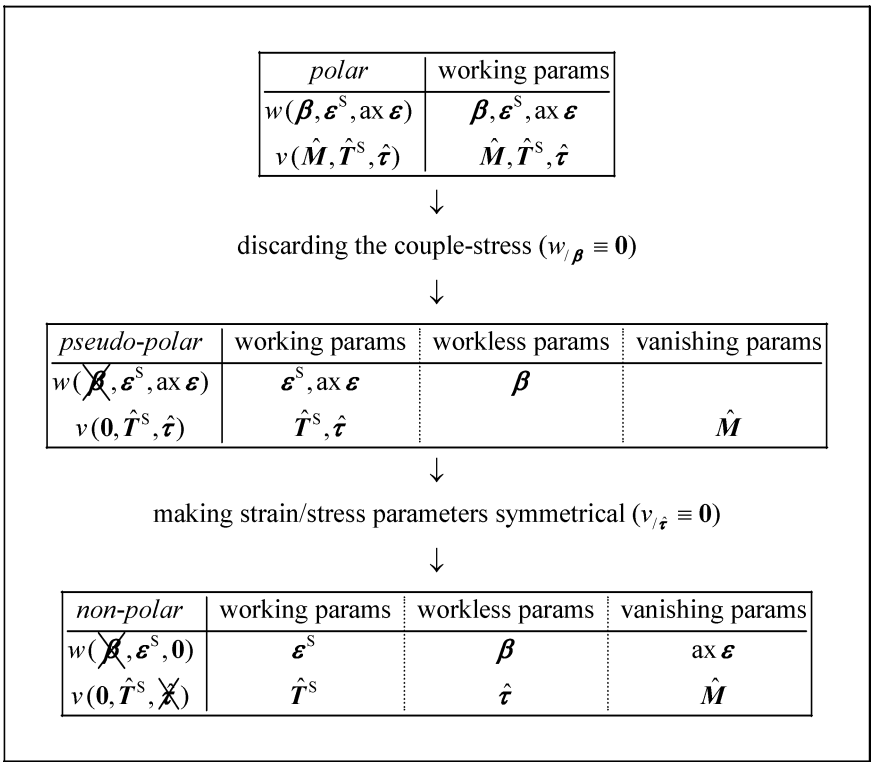

Box 1. Constitutive characterization of the non-polar medium.

$$\begin{aligned} &(\text{in } V) \quad (\boldsymbol{H}\boldsymbol{X}\hat{\boldsymbol{T}})_{/\bullet} + \boldsymbol{b} = \mathbf{0}, \\ &(\text{at } S) \quad \boldsymbol{H}\boldsymbol{X}\hat{\boldsymbol{T}}\boldsymbol{v} = \boldsymbol{s}. \end{aligned} \tag{4}$$

However, the Biot stress $\hat{\boldsymbol{T}} = \hat{\boldsymbol{T}}^{\mathrm{S}} + \hat{\boldsymbol{\tau}}\times = w_{/\boldsymbol{\varepsilon}^{\mathrm{S}}} + \hat{\boldsymbol{\tau}}\times$ is now the superposition of two parts that are uncoupled in a scalar product: an elastically determined part and a workless part to be determined statically. The internal compatibility condition $\boldsymbol{\varepsilon} = \mathrm{dual}(\boldsymbol{X}^{\mathrm{T}}\boldsymbol{H}^{\mathrm{T}}\boldsymbol{\omega})$ of the pseudo-polar medium splits into a condition on symmetric tensors,

$$\boldsymbol{\varepsilon}^{\mathrm{S}} = \mathrm{dual}(\boldsymbol{X}^{\mathrm{T}}\boldsymbol{H}^{\mathrm{T}}\boldsymbol{\omega})^{\mathrm{S}} \tag{5}$$

and into a *kinematical constraint equation*,

$$\mathrm{ax}\ \mathrm{dual}(\boldsymbol{X}^{\mathrm{T}}\boldsymbol{H}^{\mathrm{T}}\boldsymbol{\omega}) = \mathbf{0}. \tag{6}$$

The boundary compatibility condition Eq. (63) of Part I is still valid in the original form,

$$\log \boldsymbol{H} = \log \boldsymbol{H}_{\mathrm{b}}. \tag{7}$$

The proposed model of non-polar medium is better understood from the self-based standpoint. Premultiplying Eq. $(4)_1$ by $\boldsymbol{X}'^{\mathrm{T}}$ and writing the primal and dual part separately, the linear and angular balance equations within the body are obtained. Recalling Eqs. (44) and (48) of Part I, these balance equations and the kinematical constraint Eq. (6) are brought to the form

$$(\boldsymbol{\Phi}\hat{\boldsymbol{T}})_{/\bullet} + \boldsymbol{f} = \mathbf{0}, \quad 2\mathrm{ax}(\boldsymbol{\Phi}\hat{\boldsymbol{T}}\boldsymbol{F}^{\mathrm{T}}) + \boldsymbol{c} = \mathbf{0}, \quad \mathrm{ax}(\boldsymbol{\Phi}^{\mathrm{T}}\boldsymbol{F}) = \mathbf{0}. \tag{8}$$

Eqs. (8) are the genuine equations governing the present model of non-polar hyperelastic medium. Once $\hat{\boldsymbol{T}} = w_{/\boldsymbol{\varepsilon}^{\mathrm{S}}} + \hat{\boldsymbol{\tau}}\times$ and $\boldsymbol{\varepsilon}^{\mathrm{S}} = (\boldsymbol{\Phi}^{\mathrm{T}}\boldsymbol{F})^{\mathrm{S}} - \boldsymbol{I}$ are understood, the unknown fields reduce to the position vector $\boldsymbol{x}'$, the orientation $\boldsymbol{\alpha}'$ (or equivalently the rotation $\boldsymbol{\Phi} = \boldsymbol{\alpha}'\boldsymbol{\alpha}^{\mathrm{T}}$), and the Biot-axial $\hat{\boldsymbol{\tau}}$. The algebraic Eq. $(8)_2$ simply states how a possible field of external couples of density $\boldsymbol{c}|\boldsymbol{F}|^{-1}$ per unit deformed volume is exactly balanced by the opposite of the axial vector of the analog of the Cauchy stress tensor $|\boldsymbol{F}|^{-1}\boldsymbol{\Phi}\hat{\boldsymbol{T}}\boldsymbol{F}^{\mathrm{T}}$. The presence of external body couples affects the analog of the first Piola–Kirchhoff stress tensor $\tilde{\boldsymbol{T}} = \boldsymbol{\Phi}\hat{\boldsymbol{T}}$, and, in turn, affects both the elastically determined part and the statically determined part of the Biot stress $\hat{\boldsymbol{T}}$, and, finally, the displacement field. When the external couples are absent, the analog of the Cauchy stress tensor is symmetrical and coincides with the Cauchy stress tensor defined in classical elasticity; however, the Biot stress keeps on being in general non-symmetric, i.e. the Biot-axial $\hat{\boldsymbol{\tau}}$ is in general non-null. What the particle orientation does mean in a non-polar medium in the absence of external couples can be a worthy issue. The answer can be found in Eq. $(8)_3$, which represents a statement of the polar decomposition theorem of the deformation gradient. In fact, this equation may be understood as the definition of the rotation $\boldsymbol{\Phi}$ and gives physical significance to the model of non-polar medium in the absence of external couples.

By itself, the non-polar medium so far discussed coincides with the classical medium unable of couple-stressing: in the proposed model, the presence of couple loads does not influence the constitutive law of the medium itself, but will affect its response. As for the classical medium, in the present medium the strain energy depends on six scalars, and to make it dependent on the Green strain tensor or on the strain tensor $\boldsymbol{\varepsilon}^{\mathrm{S}}$ is just a matter of choice of parameterization. The non-polar medium is best described via the triplet of Eqs. (8), however it can also be described by means of just the linear balance equation with the only unknown $\boldsymbol{x}'$ from a Green-type parameterization of the strain energy, after assuming as fulfilled the angular balance equation and the kinematical constraint, and correspondingly losing any trace of the rotation and Biot-axial fields. This particularization of the non-polar model was discussed by Merlini (1997) within the framework of a consistent variational formulation, and the ensuing model was shown to be able to work also under possible external body couples. Of course, the external couples will influence the stress distribution and the kinematical response.

3.2. Variational principles

The derivation of the variational principles for the non-polar medium in the context of the helicoidal modeling closely follows the framework established in Part I for the polar case, and is based on a set of scalar equations equivalent to the governing equations. For convenience, we maintain the mnemonics 'three-field', 'two-field' and 'one-field' for the corresponding formulations. From Eqs. (3)–(7), the scalar equations of the full, three-field formulation can be written as (see Eqs. (64) in Part I)

$$
\begin{aligned}
&(\text{in } V) \quad \begin{cases} \langle \boldsymbol{a}'_{\delta}, (\boldsymbol{H}\boldsymbol{X}\hat{\boldsymbol{T}})_{/\bullet} + \boldsymbol{b}\rangle - \langle \delta\hat{\boldsymbol{\tau}}, \text{dual } 2\ \text{ax}(\boldsymbol{X}^{\mathrm{T}}\boldsymbol{H}^{\mathrm{T}}\boldsymbol{\omega})\rangle = 0, \\ \langle \delta\boldsymbol{\varepsilon}^{\mathrm{S}}, \hat{\boldsymbol{T}}^{\mathrm{S}} - w_{/\boldsymbol{\varepsilon}^{\mathrm{S}}}\rangle = 0, \\ \langle \delta\hat{\boldsymbol{T}}^{\mathrm{S}}, \boldsymbol{\varepsilon}^{\mathrm{S}} - \text{dual}(\boldsymbol{X}^{\mathrm{T}}\boldsymbol{H}^{\mathrm{T}}\boldsymbol{\omega})^{\mathrm{S}}\rangle = 0, \end{cases} \\
&(\text{at } S) \quad \begin{cases} \langle \boldsymbol{a}'_{\delta}, -\boldsymbol{H}\boldsymbol{X}\hat{\boldsymbol{T}}\boldsymbol{v} + \boldsymbol{s}\rangle = 0, \\ \langle \delta(\boldsymbol{\Lambda}\boldsymbol{X}\hat{\boldsymbol{T}}\boldsymbol{v}), \text{ax}(\log\boldsymbol{H} - \log\boldsymbol{H}_{\mathrm{b}})\rangle = 0, \end{cases}
\end{aligned}
\tag{9}
$$

with $\hat{\boldsymbol{T}}$ a short form of $\hat{\boldsymbol{T}}^{\mathrm{S}} + \hat{\boldsymbol{\tau}}\times$. Note that the kinematical constraint is understood as a primary governing equation besides the internal balance, and the relevant scalar equations are deliberately summed up within a single line in Eq. $(9)_1$. The unknowns are the parameters describing the current oriento-position $\boldsymbol{A}'$ together with the Biot-axial $\hat{\boldsymbol{\tau}}$, and the strain and stress parameters $\boldsymbol{\varepsilon}^{\mathrm{S}}$ and $\hat{\boldsymbol{T}}^{\mathrm{S}}$.

Following the standard schemes of the calculus of variations, Eqs. (9) are integrated over the relevant domains, then appropriate scalar products are transferred from volume to surface integrals by means of the divergence theorem. The details of the derivation can be found in the analogous formulation of Part I: as discussed there, according to how many scalar products are transferred to the surface domain, three levels of variational forms are obtained, referred to as the weak, the weaker and the weakest variational form, respectively. The weak and the weakest forms are almost identical to those of the polar medium (Eqs. (66) and (68) in Part I). The intermediate, or weaker form (see Eq. (67) in Part I) gives rise to the *Three-field Principle*

$$\int_V \delta[w + \langle \hat{\boldsymbol{\tau}}, \text{dual } 2 \text{ ax}(\boldsymbol{X}^{\mathrm{T}}\boldsymbol{H}^{\mathrm{T}}\boldsymbol{\omega})\rangle - \langle \hat{\boldsymbol{T}}^{\mathrm{S}}, \boldsymbol{\varepsilon}^{\mathrm{S}} - \text{dual}(\boldsymbol{X}^{\mathrm{T}}\boldsymbol{H}^{\mathrm{T}}\boldsymbol{\omega})^{\mathrm{S}}\rangle]\,\mathrm{d}V$$
$$= \int_V \langle \boldsymbol{a}'_\delta, \boldsymbol{b}\rangle\,\mathrm{d}V + \int_{S_\mathrm{f}} \langle \boldsymbol{a}'_\delta, \boldsymbol{s}\rangle\,\mathrm{d}S_\mathrm{f} + \int_{S_\mathrm{c}} \{\langle \boldsymbol{a}'_\delta, \boldsymbol{s}_\mathrm{c}\rangle + \langle \delta(\boldsymbol{\Lambda}^{\mathrm{T}}\boldsymbol{s}_\mathrm{c}), \text{ax log}\,\boldsymbol{H} - \text{ax log}\,\boldsymbol{H}_\mathrm{c}\rangle\}\,\mathrm{d}S_\mathrm{c}, \tag{10}$$

and, using the Legendre transform $v = \langle \hat{\boldsymbol{T}}^{\mathrm{S}}, \boldsymbol{\varepsilon}^{\mathrm{S}}\rangle - w$, to the *Two-field Principle*

$$\int_V \delta[\langle \hat{\boldsymbol{T}}^{\mathrm{S}}, \text{dual}(\boldsymbol{X}^{\mathrm{T}}\boldsymbol{H}^{\mathrm{T}}\boldsymbol{\omega})^{\mathrm{S}}\rangle - v + \langle \hat{\boldsymbol{\tau}}, \text{dual } 2 \text{ ax}(\boldsymbol{X}^{\mathrm{T}}\boldsymbol{H}^{\mathrm{T}}\boldsymbol{\omega})\rangle]\,\mathrm{d}V$$
$$= \int_V \langle \boldsymbol{a}'_\delta, \boldsymbol{b}\rangle\,\mathrm{d}V + \int_{S_\mathrm{f}} \langle \boldsymbol{a}'_\delta, \boldsymbol{s}\rangle\,\mathrm{d}S_\mathrm{f} + \int_{S_\mathrm{c}} \{\langle \boldsymbol{a}'_\delta, \boldsymbol{s}_\mathrm{c}\rangle + \langle \delta(\boldsymbol{\Lambda}^{\mathrm{T}}\boldsymbol{s}_\mathrm{c}), \text{ax log}\,\boldsymbol{H} - \text{ax log}\,\boldsymbol{H}_\mathrm{c}\rangle\}\,\mathrm{d}S_\mathrm{c}, \tag{11}$$

which has as primary unknowns the parameters of $\boldsymbol{A}'$ together with $\hat{\boldsymbol{\tau}}$, and the stress parameter $\hat{\boldsymbol{T}}^{\mathrm{S}}$. Note that in Eqs. (10) and (11), the surface constraints are accounted for as a weak statement and introduce the reaction density $\boldsymbol{s}_c$ as a possible boundary unknown. These principles correspond respectively to the well-known principles of Hu–Washizu and of Hellinger–Reissner, and are the most general principles in finite elasticity mechanics of a non-polar medium in the context of the helicoidal modeling.

From the three-field formulation, by forcing as an identity $\boldsymbol{\varepsilon}^{\mathrm{S}} \equiv \text{dual}(\boldsymbol{X}^{\mathrm{T}}\boldsymbol{H}^{\mathrm{T}}\boldsymbol{\omega})^{\mathrm{S}}$ and by implicitly assuming $\hat{\boldsymbol{T}}^{\mathrm{S}} \equiv w_{/\boldsymbol{\varepsilon}^{\mathrm{S}}}$, the *One-field Principle* descends,

$$\int_V \delta[w + \langle \hat{\boldsymbol{\tau}}, \text{dual } 2 \text{ ax}(\boldsymbol{X}^{\mathrm{T}}\boldsymbol{H}^{\mathrm{T}}\boldsymbol{\omega})\rangle]\,\mathrm{d}V$$
$$= \int_V \langle \boldsymbol{a}'_\delta, \boldsymbol{b}\rangle\,\mathrm{d}V + \int_{S_\mathrm{f}} \langle \boldsymbol{a}'_\delta, \boldsymbol{s}\rangle\,\mathrm{d}S_\mathrm{f} + \int_{S_\mathrm{c}} \{\langle \boldsymbol{a}'_\delta, \boldsymbol{s}_\mathrm{c}\rangle + \langle \delta(\boldsymbol{\Lambda}^{\mathrm{T}}\boldsymbol{s}_\mathrm{c}), \text{ax log}\,\boldsymbol{H} - \text{ax log}\,\boldsymbol{H}_\mathrm{c}\rangle\}\,\mathrm{d}S_\mathrm{c}, \tag{12}$$

with the parameters of $\boldsymbol{A}'$ together with the Biot-axial $\hat{\boldsymbol{\tau}}$ as primary field unknowns, and the constraint reaction $\boldsymbol{s}_c$ as the boundary unknown. By forcing as an identity the boundary compatibility $\log \boldsymbol{H} \equiv \log \boldsymbol{H}_\mathrm{c}$ as well, the boundary unknown $\boldsymbol{s}_c$ disappears and the *Principle of Virtual Work* is written in the internally constrained form $\int_V \delta[w + \langle \hat{\boldsymbol{\tau}}, \text{dual } 2 \text{ ax}(\boldsymbol{X}^{\mathrm{T}}\boldsymbol{H}^{\mathrm{T}}\boldsymbol{\omega})\rangle]\,\mathrm{d}V = \int_V \langle \boldsymbol{a}'_\delta, \boldsymbol{b}\rangle\,\mathrm{d}V + \int_{S_\mathrm{f}} \langle \boldsymbol{a}'_\delta, \boldsymbol{s}\rangle\,\mathrm{d}S_\mathrm{f}$.

3.3. Linearization

The variational principles above are linearized following the guidelines given in Part I. Here, we limit ourselves to the linearization of the One-field Principle, Eq. (12), under the simplifying hypothesis of constant density fields of the self-based external loads $\boldsymbol{X}'^{\mathrm{T}}\boldsymbol{b}$ and $\boldsymbol{X}'^{\mathrm{T}}\boldsymbol{s}$. This leads to the incremental form $\Pi_\delta + \partial\Pi_\delta = 0$, where

$$\Pi_\delta = \int_V \{\langle \boldsymbol{A}'\delta(\boldsymbol{A}'^{\mathrm{T}}\boldsymbol{k}'), \tilde{\boldsymbol{S}}\rangle + \langle \delta\hat{\boldsymbol{\tau}}\times, \boldsymbol{\Phi}^{\mathrm{T}}\text{dual}(\boldsymbol{X}'^{\mathrm{T}}\boldsymbol{\omega})\rangle\}\,\mathrm{d}V$$
$$- \int_V \langle \boldsymbol{X}'^{\mathrm{T}}\boldsymbol{a}'_\delta, \boldsymbol{X}'^{\mathrm{T}}\boldsymbol{b}\rangle\,\mathrm{d}V - \int_{S_\mathrm{f}} \langle \boldsymbol{X}'^{\mathrm{T}}\boldsymbol{a}'_\delta, \boldsymbol{X}'^{\mathrm{T}}\boldsymbol{s}\rangle\,\mathrm{d}S_\mathrm{f} + \Pi_{\delta S_\mathrm{c}}, \tag{13}$$
$$\partial\Pi_\delta = \partial\Pi_{\delta E} + \partial\Pi_{\delta K} + \partial\Pi_{\delta G} + \partial\Pi_{\delta S_\mathrm{c}},$$

with $\Pi_{\delta S_c}$ and $\partial\Pi_{\delta S_c}$ the contributions from the constrained boundary, and

$$\begin{aligned}
\partial\Pi_{\delta E} &= \int_V \boldsymbol{\Phi}^{\mathrm{T}}\mathrm{dual}(\boldsymbol{X}'^{\mathrm{T}}\boldsymbol{A}'\delta(\boldsymbol{A}'^{\mathrm{T}}\boldsymbol{k}')) : \ \mathbb{E}_{\mathrm{g}^{\mathrm{S}}\mathrm{g}^{\mathrm{S}}} : \boldsymbol{\Phi}^{\mathrm{T}}\mathrm{dual}(\boldsymbol{X}'^{\mathrm{T}}\boldsymbol{A}'\partial(\boldsymbol{A}'^{\mathrm{T}}\boldsymbol{k}'))\,\mathrm{d}V,\\
\partial\Pi_{\delta K} &= \int_V \{\langle\delta\hat{\boldsymbol{\tau}}\times, \boldsymbol{\Phi}^{\mathrm{T}}\mathrm{dual}(\boldsymbol{X}'^{\mathrm{T}}\boldsymbol{A}'\partial(\boldsymbol{A}'^{\mathrm{T}}\boldsymbol{k}'))\rangle + \langle\partial\hat{\boldsymbol{\tau}}\times, \boldsymbol{\Phi}^{\mathrm{T}}\mathrm{dual}(\boldsymbol{X}'^{\mathrm{T}}\boldsymbol{A}'\delta(\boldsymbol{A}'^{\mathrm{T}}\boldsymbol{k}'))\rangle\\
&\quad + \langle\partial\delta\hat{\boldsymbol{\tau}}\times, \boldsymbol{\Phi}^{\mathrm{T}}\mathrm{dual}(\boldsymbol{X}'^{\mathrm{T}}\boldsymbol{\omega})\rangle\}\,\mathrm{d}V,\\
\partial\Pi_{\delta G} &= \int_V \langle\boldsymbol{A}'\partial\delta(\boldsymbol{A}'^{\mathrm{T}}\boldsymbol{k}'), \tilde{\boldsymbol{S}}\rangle\,\mathrm{d}V - \int_V \langle\partial(\boldsymbol{X}'^{\mathrm{T}}\boldsymbol{a}'_{\delta}), \boldsymbol{X}'^{\mathrm{T}}\boldsymbol{b}\rangle\,\mathrm{d}V - \int_{S_{\mathrm{f}}} \langle\partial(\boldsymbol{X}'^{\mathrm{T}}\boldsymbol{a}'_{\delta}), \boldsymbol{X}'^{\mathrm{T}}\boldsymbol{s}\rangle\,\mathrm{d}S_{\mathrm{f}}.
\end{aligned} \tag{14}$$

The contribution $\partial\Pi_{\delta K}$ is peculiar to the non-polar medium and accounts for the internal kinematical constraint, Eq. (6). The expression of the geometric contribution $\partial\Pi_{\delta G}$ is the same as for the polar medium, Eq. $(75)_2$ of Part I. The linearization of the contribution $\Pi_{\delta S_c}$ is not attempted in this paper (see discussion in Part I, Section 5.5). By discarding the contributions $\Pi_{\delta S_c}$ and $\partial\Pi_{\delta S_c}$, the linearized form of the Constrained Principle of Virtual Work is obtained.

The linearized virtual functional depends, besides on the free variables $\boldsymbol{A}'$, $\hat{\boldsymbol{\tau}}$, on the relevant virtual, incremental and mixed virtual–incremental variables, namely the differential oriento-position dual vectors and curvature dual tensors $\boldsymbol{a}'_{\delta}$, $\boldsymbol{a}'_{\partial}$, $\boldsymbol{a}'_{\partial\delta}$, $\boldsymbol{k}'_{\delta}$, $\boldsymbol{k}'_{\partial}$, $\boldsymbol{k}'_{\partial\delta}$ (see Part I), and the Biot-axial variations $\delta\hat{\boldsymbol{\tau}}$, $\partial\hat{\boldsymbol{\tau}}$, $\partial\delta\hat{\boldsymbol{\tau}}$. We wish to point out that the mixed virtual–incremental variables cannot be discarded a priori in finite-element approximations of nonlinear mechanics, unless the field variables are assumed to be linearly dependent on the discrete set of the global analysis variables. In fact, the linearization of the variational principle is actually performed with respect to the truly free problem variables, and as we shall exploit nonlinear finite elements in the next approximation, it is clear that the local mixed variation variables must be retained in the linearized principle (see also Part II, Section 4.1).

It is now worth comparing the linearized Constrained Principle of Virtual Work as obtained under the helicoidal modeling with that obtained under classical modeling (Merlini, 1997). After some manipulations, Eqs. (13) can be brought to a form comparable with the linearized functional from the classical modeling: the scalar products between dual tensors can be resolved into products between real tensors using Eq. (55), Part I; then, the following formulae can be exploited, as obtained from the kinematics detailed in Part I, $\mathrm{dual}(\boldsymbol{X}'^{\mathrm{T}}\boldsymbol{A}'\partial(\boldsymbol{A}'^{\mathrm{T}}\boldsymbol{k}')) = \boldsymbol{\Phi}\partial(\boldsymbol{\Phi}^{\mathrm{T}}\boldsymbol{F})$, $\mathrm{dual}(\boldsymbol{X}'^{\mathrm{T}}\boldsymbol{A}'\partial\delta(\boldsymbol{A}'^{\mathrm{T}}\boldsymbol{k}')) = \boldsymbol{\Phi}\partial\delta(\boldsymbol{\Phi}^{\mathrm{T}}\boldsymbol{F})$, $\mathrm{primal}(\boldsymbol{X}'^{\mathrm{T}}\boldsymbol{a}'_{\delta}) = \boldsymbol{\varphi}_{\delta}$, $\mathrm{dual}(\boldsymbol{X}'^{\mathrm{T}}\boldsymbol{a}'_{\delta}) = \delta\boldsymbol{x}'$, $\mathrm{primal}\,\partial(\boldsymbol{X}'^{\mathrm{T}}\boldsymbol{a}'_{\delta}) = \boldsymbol{\varphi}_{\partial\delta} + \frac{1}{2}\boldsymbol{\varphi}_{\partial}\times\boldsymbol{\varphi}_{\delta}$ (see Eq. (20) below), $\mathrm{dual}\,\partial(\boldsymbol{X}'^{\mathrm{T}}\boldsymbol{a}'_{\delta}) = \partial\delta\boldsymbol{x}'$. By doing so, one arrives at the same constrained virtual functional proposed by Merlini (1997), but one would fail to obtain the same linearized form, unless the mixed virtual–incremental multipliers $\partial\delta\boldsymbol{x}'$ and $\partial\delta\boldsymbol{F}$ are discarded. Indeed, such mixed variation variables are customarily discarded in classical modeling using linear finite element approximations, but this is not feasible under the helicoidal modeling. In the latter, the truly free variables are the dual parameters of the rototranslation field, and differential helices control the tangent space of this kind of field. As discussed in Part I, Section 4.2, the linear part of such differential helices is quite different from the Euclidean differential of the position vector. Remember that the helicoidal modeling is based on kinematical variables that are a nonlinear transformation of the classical kinematical variables; so, when linearizing the virtual functional, the mixed variation variables $\partial\delta\boldsymbol{x}'$ and $\partial\delta\boldsymbol{F}$ ought to be retained as non-null quantities. Therefore, the differences in the tangent space of the two kinds of variable fields infer different tangent maps for the variational principle.

4. Finite element approximation

The approximation by finite elements concerns the linearized One-field Principle in the form of the Constrained Principle of Virtual Work, as obtained by discarding the contribution from the boundary

constraints in Eqs. (13). Moreover, in the approximated version of the linearized principle, we also explicitly consider a particular form of boundary loads in order to account for possible *follower forces*, i.e. forces that locally rotate and maintain the relative orientation against the deformed surface. This feature proves useful when analyzing highly deforming bodies under pressure loading. In this work, we denote by $\boldsymbol{s}_{\mathrm{F}} = \boldsymbol{X}'\boldsymbol{t}_{\mathrm{F}}$ the pole-based surface density of an external follower force, and augment the virtual functional Π_δ by the surface work term $\langle \boldsymbol{X}'^{\mathrm{T}}\boldsymbol{a}'_\delta, \boldsymbol{\Phi}\boldsymbol{X}'^{\mathrm{T}}\boldsymbol{s}_{\mathrm{F}}\rangle$, where the self-based force density $\boldsymbol{t}_{\mathrm{F}} = \boldsymbol{X}'^{\mathrm{T}}\boldsymbol{s}_{\mathrm{F}}$ is assumed to be a constant vector. The linearization of this term yields the additional surface term $\langle \partial(\boldsymbol{X}'^{\mathrm{T}}\boldsymbol{a}'_\delta), \boldsymbol{\Phi}\boldsymbol{X}'^{\mathrm{T}}\boldsymbol{s}_{\mathrm{F}}\rangle - \langle \boldsymbol{X}'^{\mathrm{T}}\boldsymbol{a}'_\delta, (\boldsymbol{\Phi}\boldsymbol{X}'^{\mathrm{T}}\boldsymbol{s}_{\mathrm{F}}) \times \boldsymbol{\varphi}_\partial\rangle$ in the geometric contribution $\partial\Pi_{\delta G}$.

4.1. Formulation of the element matrices

To establish a finite element approximation, the body volume and the loaded boundary surface are subdivided into volume elements V^e and free-surface elements S^e_{f}, respectively. Therefore, the virtual functional and its variation are assembled with the contributions from the single elements,

$$\begin{aligned} \Pi_\delta &= \sum_{V^e} \Pi^{V^e}_\delta + \sum_{S^e_{\mathrm{f}}} \Pi^{S^e_{\mathrm{f}}}_\delta, \\ \partial\Pi_\delta &= \sum_{V^e} \left(\partial\Pi^{V^e}_{\delta E} + \partial\Pi^{V^e}_{\delta K} + \partial\Pi^{V^e}_{\delta G}\right) + \sum_{S^e_{\mathrm{f}}} \partial\Pi^{S^e_{\mathrm{f}}}_{\delta G}. \end{aligned} \tag{15}$$

The use of dedicated surface load elements is perhaps a non-standard practice in the finite element method and is an alternative to equip solid elements with face-loading features. Since such elements are perfectly compatible with the adjacent solid elements (see Section 5.1), they represent a very flexible way of introducing distributed surface loads on volume elements based on nonlinear interpolating functions. Note that the surface elements contribute to the geometric tangent matrix, see Eq. $(14)_3$.

Each contribution in Eqs. (15) is a functional of proper substitute fields of the free variables and of the relevant variation variables, defined over the element domain; so, it approximates the true contribution from the pertinent body or boundary region. The kinematical substitute field of the particle oriento-positions $\boldsymbol{A}'$ is based on the multiplicative interpolation scheme discussed in Part II, and is governed by the implicit nonlinear equation

$$\sum_{J=1}^{N} W_J \log(\boldsymbol{A}'\boldsymbol{A}'^{\mathrm{T}}_J) = \boldsymbol{0}, \tag{16}$$

where W_J are scalar weight functions. The Biot-axial $\hat{\boldsymbol{\tau}}$ is meant to belong to the Euclidean vector space, and in the present formulation the relevant substitute field is based on an additive, explicit and linear interpolation formula of the kind

$$\hat{\boldsymbol{\tau}} = \sum_{J=1}^{F} \boldsymbol{\Sigma}_J \cdot \hat{\boldsymbol{\tau}}_J, \tag{17}$$

with $\boldsymbol{\Sigma}_J$ appropriate weighing tensor functions. In Eq. (16), the N dual tensors $\boldsymbol{A}'_J$ are the nodal oriento-positions of the element, which belong to the discrete set of the global kinematical variables. In Eq. (17), vectors $\hat{\boldsymbol{\tau}}_J$ are F elements of the discrete set of the global Biot-axial variables, and are not necessarily associated with the nodes of the finite element model. The definition of the substitute fields will be completed later, when discussing the shape of the elements used.

The element contributions in Eqs. (15) are conveniently cast in explicit form, involving scalar products between real tensors. From Eqs. (13), by discarding the contribution from the boundary constraints and

accounting for possible follower forces, and also discarding, according to linear Eq. (17), the mixed variations $\partial\delta\hat{\boldsymbol{\tau}}$ of the Biot-axial field (remember that the variational principle was linearized with respect to variables $\hat{\boldsymbol{\tau}}_J$, while the $\delta\hat{\boldsymbol{\tau}}_J$ are a fully independent set of arbitrary variables), we can write, for the volume element

$$\begin{aligned}
\Pi^{Ve}_{\delta} &= \int_{Ve} \{\mathrm{dual}(\boldsymbol{X}'^{\mathrm{T}}\boldsymbol{A}'\delta(\boldsymbol{A}'^{\mathrm{T}}\boldsymbol{k}')) : \tilde{\boldsymbol{T}} + \delta\hat{\boldsymbol{\tau}}\times : \boldsymbol{\Phi}^{\mathrm{T}}\mathrm{dual}(\boldsymbol{X}'^{\mathrm{T}}\boldsymbol{\omega}) \\
&\quad - \mathrm{primal}(\boldsymbol{X}'^{\mathrm{T}}\boldsymbol{a}'_{\delta}) \cdot \boldsymbol{c} - \mathrm{dual}(\boldsymbol{X}'^{\mathrm{T}}\boldsymbol{a}'_{\delta}) \cdot \boldsymbol{f}\ \}\,\mathrm{d}V^e, \\
\partial\Pi^{Ve}_{\delta E} &= \int_{Ve} \boldsymbol{\Phi}^{\mathrm{T}}\mathrm{dual}(\boldsymbol{X}'^{\mathrm{T}}\boldsymbol{A}'\delta(\boldsymbol{A}'^{\mathrm{T}}\boldsymbol{k}')) : \mathbb{E}_{\mathfrak{s}\mathfrak{s}}\mathfrak{s} : \boldsymbol{\Phi}^{\mathrm{T}}\mathrm{dual}(\boldsymbol{X}'^{\mathrm{T}}\boldsymbol{A}'\partial(\boldsymbol{A}'^{\mathrm{T}}\boldsymbol{k}'))\,\mathrm{d}V^e, \\
\partial\Pi^{Ve}_{\delta K} &= \int_{Ve} \{\delta\hat{\boldsymbol{\tau}}\times : \boldsymbol{\Phi}^{T}\mathrm{dual}(\boldsymbol{X}'^{\mathrm{T}}\boldsymbol{A}'\partial(\boldsymbol{A}'^{\mathrm{T}}\boldsymbol{k}')) + \boldsymbol{\Phi}^{\mathrm{T}}\mathrm{dual}(\boldsymbol{X}'^{\mathrm{T}}\boldsymbol{A}'\delta(\boldsymbol{A}'^{T}\boldsymbol{k}')) : \partial\hat{\boldsymbol{\tau}}\times\}\,\mathrm{d}V^e, \\
\partial\Pi^{Ve}_{\delta G} &= \int_{Ve} \{\mathrm{dual}(\boldsymbol{X}'^{\mathrm{T}}\boldsymbol{A}'\partial\delta(\boldsymbol{A}'^{\mathrm{T}}\boldsymbol{k}')) : \tilde{\boldsymbol{T}} - \mathrm{primal}\,\partial(\boldsymbol{X}'^{\mathrm{T}}\boldsymbol{a}'_{\delta}) \cdot \boldsymbol{c} - \mathrm{dual}\,\partial(\boldsymbol{X}'^{\mathrm{T}}\boldsymbol{a}'_{\delta}) \cdot \boldsymbol{f}\ \}\,\mathrm{d}V^e,
\end{aligned} \tag{18}$$

with $\tilde{\boldsymbol{T}} = \boldsymbol{\Phi}(\hat{\boldsymbol{T}}^{\mathrm{S}} + \hat{\boldsymbol{\tau}}\times)$, and for the surface element

$$\begin{aligned}
\Pi^{S^e_{\mathrm{f}}}_{\delta} &= \int_{S^e_{\mathrm{f}}} \{-\mathrm{dual}(\boldsymbol{X}'^{\mathrm{T}}\boldsymbol{a}'_{\delta}) \cdot (\boldsymbol{t} + \boldsymbol{\Phi}\boldsymbol{t}_{\mathrm{F}})\}\,\mathrm{d}S^e_{\mathrm{f}}, \\
\partial\Pi^{S^e_{\mathrm{f}}}_{\delta G} &= \int_{S^e_{\mathrm{f}}} \{-\mathrm{dual}\,\partial(\boldsymbol{X}'^{\mathrm{T}}\boldsymbol{a}'_{\delta}) \cdot (\boldsymbol{t} + \boldsymbol{\Phi}\boldsymbol{t}_{\mathrm{F}}) + \mathrm{dual}(\boldsymbol{X}'^{\mathrm{T}}\boldsymbol{a}'_{\delta}) \cdot (\boldsymbol{\Phi}\boldsymbol{t}_{\mathrm{F}}) \times \mathrm{primal}(\boldsymbol{X}'^{\mathrm{T}}\boldsymbol{a}'_{\partial})\}\,\mathrm{d}S^e_{\mathrm{f}}.
\end{aligned} \tag{19}$$

Any variation variables involved in Eqs. (18) and (19) can be reduced to the primitive virtual ($\boldsymbol{a}'_{\delta}$, $\boldsymbol{k}'_{\delta}$, $\delta\hat{\boldsymbol{\tau}}$), incremental ($\boldsymbol{a}'_{\partial}$, $\boldsymbol{k}'_{\partial}$, $\partial\hat{\boldsymbol{\tau}}$) and mixed virtual–incremental ($\boldsymbol{a}'_{\partial\delta}$, $\boldsymbol{k}'_{\partial\delta}$) variables (refer to the co-rototranslational variation formulae, Eqs. (42) of Part I). In particular, the following explicit expression for the multiplier $\partial(\boldsymbol{X}'^{\mathrm{T}}\boldsymbol{a}'_{\delta})$ of the external loads in the incremental term is obtained (Merlini and Morandini, 2004b),

$$\begin{aligned}
\partial(\boldsymbol{X}'^{\mathrm{T}}\boldsymbol{a}'_{\delta}) &= \boldsymbol{X}'^{\mathrm{T}}\boldsymbol{a}'_{\partial\delta} + \frac{1}{2}\mathrm{primal}(\boldsymbol{X}'^{\mathrm{T}}\boldsymbol{a}'_{\partial}) \times \mathrm{primal}(\boldsymbol{X}'^{\mathrm{T}}\boldsymbol{a}'_{\delta}) \\
&\quad + \varepsilon\,\frac{1}{2}(\mathrm{primal}(\boldsymbol{X}'^{\mathrm{T}}\boldsymbol{a}'_{\partial}) \times \mathrm{dual}(\boldsymbol{X}'^{\mathrm{T}}\boldsymbol{a}'_{\delta}) + \mathrm{primal}(\boldsymbol{X}'^{\mathrm{T}}\boldsymbol{a}'_{\delta}) \times \mathrm{dual}(\boldsymbol{X}'^{\mathrm{T}}\boldsymbol{a}'_{\partial})).
\end{aligned} \tag{20}$$

Eq. (20) clearly shows that the dual part of this multiplier is symmetrical with respect to virtual and incremental variations, while the primal part is not. Note that the mixed virtual–incremental kinematical variables are supported by the multiplicative interpolation and are not solved locally for the virtual and the incremental variables separately.

In order to formulate the element matrices, we need to evaluate any variation variables in Eqs. (18) and (19) as a linear function of the variation variables relevant to the discrete set of the global model variables. The last are the virtual, incremental and mixed virtual–incremental nodal oriento-position dual vectors $\boldsymbol{a}'_{\delta J}$, $\boldsymbol{a}'_{\partial J}$, $\boldsymbol{a}'_{\partial\delta J}$, and the virtual and incremental variations $\delta\hat{\boldsymbol{\tau}}_J$, $\partial\hat{\boldsymbol{\tau}}_J$ of the global Biot-axial variables. The required relations are supplied by the primitive interpolation formulae, Eqs. (14) and (16) of Part II, and by the obvious formula $\delta\hat{\boldsymbol{\tau}} = \sum \boldsymbol{\Sigma}_J \cdot \delta\hat{\boldsymbol{\tau}}_J$ descending from Eq. (17). Derivative interpolation formulae for the other kinematical variation variables are provided in Box 2; the relevant coefficient tensors are built with tensors available from Part II, Eqs. (17), and are listed in Box 3 (details in Merlini and Morandini, 2004b). Here, subscripts 'a' and 'l' denote the angular and linear parts, respectively, of a dual vector.

Substituting the interpolation formulae within Eqs. (18) and (19), the element contributions in Eqs. (15) are finally brought to the following forms, respectively for the volume element,

$$
\begin{array}{ll}
\text{primal}\,(\boldsymbol{X}'^{\mathrm{T}}\boldsymbol{a}'_{\delta}) & = \sum_{J=1}^{N} \boldsymbol{N}_{\mathrm{Aa\_a},J}\cdot\boldsymbol{a}'_{\mathrm{a}\delta J} \\
\text{dual}\,(\boldsymbol{X}'^{\mathrm{T}}\boldsymbol{a}'_{\delta}) & = \sum_{J=1}^{N} \boldsymbol{N}_{\mathrm{Al\_a},J}\cdot\boldsymbol{a}'_{\mathrm{a}\delta J} \\
 & \quad + \sum_{J=1}^{N} \boldsymbol{N}_{\mathrm{Al\_l},J}\cdot\boldsymbol{a}'_{\mathrm{l}\delta J} \\
\hline
\text{primal}\,\partial(\boldsymbol{X}'^{\mathrm{T}}\boldsymbol{a}'_{\delta}) & = \sum_{J=1}^{N} \boldsymbol{N}_{\mathrm{Aa\_a},J}\cdot\boldsymbol{a}'_{\mathrm{a}\partial\delta J} + \sum_{J=1}^{N}\sum_{K=1}^{N} \boldsymbol{\mathcal{N}}_{\mathrm{Aa\_aa},JK} : \boldsymbol{a}'_{\mathrm{a}\delta J}\otimes\boldsymbol{a}'_{\mathrm{a}\partial K} \\
\text{dual}\,\partial(\boldsymbol{X}'^{\mathrm{T}}\boldsymbol{a}'_{\delta}) & = \sum_{J=1}^{N} \boldsymbol{N}_{\mathrm{Al\_a},J}\cdot\boldsymbol{a}'_{\mathrm{a}\partial\delta J} + \sum_{J=1}^{N}\sum_{K=1}^{N} \boldsymbol{\mathcal{N}}_{\mathrm{Al\_aa},JK} : \boldsymbol{a}'_{\mathrm{a}\delta J}\otimes\boldsymbol{a}'_{\mathrm{a}\partial K} + \sum_{J=1}^{N}\sum_{K=1}^{N} \boldsymbol{\mathcal{N}}_{\mathrm{Al\_al},JK} : \boldsymbol{a}'_{\mathrm{a}\delta J}\otimes\boldsymbol{a}'_{\mathrm{l}\partial K} \\
 & \quad + \sum_{J=1}^{N} \boldsymbol{N}_{\mathrm{Al\_l},J}\cdot\boldsymbol{a}'_{\mathrm{l}\partial\delta J} + \sum_{J=1}^{N}\sum_{K=1}^{N} \boldsymbol{\mathcal{N}}_{\mathrm{Al\_la},JK} : \boldsymbol{a}'_{\mathrm{l}\delta J}\otimes\boldsymbol{a}'_{\mathrm{a}\partial K} \\
\hline
\text{primal}\,(\boldsymbol{X}'^{\mathrm{T}}\boldsymbol{A}'\delta(\boldsymbol{A}'^{\mathrm{T}}\boldsymbol{k}')) & = \sum_{J=1}^{N} \boldsymbol{\mathcal{N}}_{\mathrm{Ka\_a},J} : \boldsymbol{a}'_{\mathrm{a}\delta J}\otimes\boldsymbol{I} \\
\text{dual}\,(\boldsymbol{X}'^{\mathrm{T}}\boldsymbol{A}'\delta(\boldsymbol{A}'^{\mathrm{T}}\boldsymbol{k}')) & = \sum_{J=1}^{N} \boldsymbol{\mathcal{N}}_{\mathrm{Kl\_a},J} : \boldsymbol{a}'_{\mathrm{a}\delta J}\otimes\boldsymbol{I} \\
 & \quad + \sum_{J=1}^{N} \boldsymbol{\mathcal{N}}_{\mathrm{Kl\_l},J} : \boldsymbol{a}'_{\mathrm{l}\delta J}\otimes\boldsymbol{I} \\
\hline
\text{primal}\,(\boldsymbol{X}'^{\mathrm{T}}\boldsymbol{A}'\partial\delta(\boldsymbol{A}'^{\mathrm{T}}\boldsymbol{k}')) & = \sum_{J=1}^{N} \boldsymbol{\mathcal{N}}_{\mathrm{Ka\_a},J} : \boldsymbol{a}'_{\mathrm{a}\partial\delta J}\otimes\boldsymbol{I} + \sum_{J=1}^{N}\sum_{K=1}^{N} \mathbb{N}_{\mathrm{Ka\_aa},JK} \vdots \boldsymbol{a}'_{\mathrm{a}\delta J}\otimes\boldsymbol{a}'_{\mathrm{a}\partial K}\otimes\boldsymbol{I} \\
\text{dual}\,(\boldsymbol{X}'^{\mathrm{T}}\boldsymbol{A}'\partial\delta(\boldsymbol{A}'^{\mathrm{T}}\boldsymbol{k}')) & = \sum_{J=1}^{N} \boldsymbol{\mathcal{N}}_{\mathrm{Kl\_a},J} : \boldsymbol{a}'_{\mathrm{a}\partial\delta J}\otimes\boldsymbol{I} + \sum_{J=1}^{N}\sum_{K=1}^{N} \mathbb{N}_{\mathrm{Kl\_aa},JK} \vdots \boldsymbol{a}'_{\mathrm{a}\delta J}\otimes\boldsymbol{a}'_{\mathrm{a}\partial K}\otimes\boldsymbol{I} + \sum_{J=1}^{N}\sum_{K=1}^{N} \mathbb{N}_{\mathrm{Kl\_al},JK} \vdots \boldsymbol{a}'_{\mathrm{a}\delta J}\otimes\boldsymbol{a}'_{\mathrm{l}\partial K}\otimes\boldsymbol{I} \\
 & \quad + \sum_{J=1}^{N} \boldsymbol{\mathcal{N}}_{\mathrm{Kl\_l},J} : \boldsymbol{a}'_{\mathrm{l}\partial\delta J}\otimes\boldsymbol{I} + \sum_{J=1}^{N}\sum_{K=1}^{N} \mathbb{N}_{\mathrm{Kl\_la},JK} \vdots \boldsymbol{a}'_{\mathrm{l}\delta J}\otimes\boldsymbol{a}'_{\mathrm{a}\partial K}\otimes\boldsymbol{I}
\end{array}
$$

Box 2. Derivative kinematical interpolation formulae.

$$
\begin{aligned}
\Pi^{Ve}_{\delta} &= \sum_{J=1}^{N} \left\{ \begin{matrix} \boldsymbol{a}'_{\mathrm{a}\delta J} \\ \boldsymbol{a}'_{\mathrm{l}\delta J} \end{matrix} \right\}^{\mathrm{T}} \cdot \left\{ \begin{matrix} \boldsymbol{F}^{V}_{\mathrm{a}J} \\ \boldsymbol{F}^{V}_{\mathrm{l}J} \end{matrix} \right\} + \sum_{J=1}^{F} \delta\hat{\boldsymbol{\tau}}_{J}\cdot\mathbf{F}^{V}_{\tau J}, \\
\partial\Pi^{Ve}_{\delta E} &= \sum_{J=1}^{N}\sum_{K=1}^{N} \left\{ \begin{matrix} \boldsymbol{a}'_{\mathrm{a}\delta J} \\ \boldsymbol{a}'_{\mathrm{l}\delta J} \end{matrix} \right\}^{\mathrm{T}} \cdot \begin{bmatrix} \boldsymbol{K}^{V}_{E\mathrm{aa}JK} & \boldsymbol{K}^{V}_{E\mathrm{al}JK} \\ \boldsymbol{K}^{V}_{E\mathrm{la}JK} & \boldsymbol{K}^{V}_{E\mathrm{ll}JK} \end{bmatrix} \cdot \left\{ \begin{matrix} \boldsymbol{a}'_{\mathrm{a}\partial K} \\ \boldsymbol{a}'_{\mathrm{l}\partial K} \end{matrix} \right\}, \\
\partial\Pi^{Ve}_{\delta K} &= \sum_{J=1}^{F}\sum_{K=1}^{N} \delta\hat{\boldsymbol{\tau}}_{J}\cdot\begin{bmatrix} \boldsymbol{K}^{V}_{K\tau\mathrm{a}JK} & \boldsymbol{K}^{V}_{K\tau\mathrm{l}JK} \end{bmatrix} \cdot \left\{ \begin{matrix} \boldsymbol{a}'_{\mathrm{a}\partial K} \\ \boldsymbol{a}'_{\mathrm{l}\partial K} \end{matrix} \right\} + \sum_{J=1}^{N}\sum_{K=1}^{F} \left\{ \begin{matrix} \boldsymbol{a}'_{\mathrm{a}\delta J} \\ \boldsymbol{a}'_{\mathrm{l}\delta J} \end{matrix} \right\}^{\mathrm{T}} \cdot \left\{ \begin{matrix} \boldsymbol{K}^{V}_{K\mathrm{a}\tau JK} \\ \boldsymbol{K}^{V}_{K\mathrm{l}\tau JK} \end{matrix} \right\} \cdot \partial\hat{\boldsymbol{\tau}}_{K}, \\
\partial\Pi^{Ve}_{\delta G} &= \sum_{J=1}^{N} \left\{ \begin{matrix} \boldsymbol{a}'_{\mathrm{a}\partial\delta J} \\ \boldsymbol{a}'_{\mathrm{l}\partial\delta J} \end{matrix} \right\}^{\mathrm{T}} \cdot \left\{ \begin{matrix} \boldsymbol{F}^{V}_{\mathrm{a}J} \\ \boldsymbol{F}^{V}_{\mathrm{l}J} \end{matrix} \right\} + \sum_{J=1}^{N}\sum_{K=1}^{N} \left\{ \begin{matrix} \boldsymbol{a}'_{\mathrm{a}\delta J} \\ \boldsymbol{a}'_{\mathrm{l}\delta J} \end{matrix} \right\}^{\mathrm{T}} \cdot \begin{bmatrix} \boldsymbol{K}^{V}_{G\mathrm{aa}JK} & \boldsymbol{K}^{V}_{G\mathrm{al}JK} \\ \boldsymbol{K}^{V}_{G\mathrm{la}JK} & \mathbf{0} \end{bmatrix} \cdot \left\{ \begin{matrix} \boldsymbol{a}'_{\mathrm{a}\partial K} \\ \boldsymbol{a}'_{\mathrm{l}\partial K} \end{matrix} \right\}
\end{aligned}
\tag{21}
$$

and for the surface element,

$$
\begin{aligned}
\Pi^{S^{e}_{\mathrm{f}}}_{\delta} &= \sum_{J=1}^{N} \left\{ \begin{matrix} \boldsymbol{a}'_{\mathrm{a}\delta J} \\ \boldsymbol{a}'_{\mathrm{l}\delta J} \end{matrix} \right\}^{\mathrm{T}} \cdot \left\{ \begin{matrix} \boldsymbol{F}^{S}_{\mathrm{a}J} \\ \boldsymbol{F}^{S}_{\mathrm{l}J} \end{matrix} \right\}, \\
\partial\Pi^{S^{e}_{\mathrm{f}}}_{\delta G} &= \sum_{J=1}^{N} \left\{ \begin{matrix} \boldsymbol{a}'_{\mathrm{a}\partial\delta J} \\ \boldsymbol{a}'_{\mathrm{l}\partial\delta J} \end{matrix} \right\}^{\mathrm{T}} \cdot \left\{ \begin{matrix} \boldsymbol{F}^{S}_{\mathrm{a}J} \\ \boldsymbol{F}^{S}_{\mathrm{l}J} \end{matrix} \right\} + \sum_{J=1}^{N}\sum_{K=1}^{N} \left\{ \begin{matrix} \boldsymbol{a}'_{\mathrm{a}\delta J} \\ \boldsymbol{a}'_{\mathrm{l}\delta J} \end{matrix} \right\}^{\mathrm{T}} \cdot \begin{bmatrix} \boldsymbol{K}^{S}_{G\mathrm{aa}JK} & \boldsymbol{K}^{S}_{G\mathrm{al}JK} \\ \boldsymbol{K}^{S}_{G\mathrm{la}JK} & \mathbf{0} \end{bmatrix} \cdot \left\{ \begin{matrix} \boldsymbol{a}'_{\mathrm{a}\partial K} \\ \boldsymbol{a}'_{\mathrm{l}\partial K} \end{matrix} \right\}.
\end{aligned}
\tag{22}
$$

$$
\begin{array}{ll}
\boldsymbol{N}_{\mathrm{Aa\_a}J} & = \mathrm{primal}\,(\boldsymbol{X}'^{\mathrm{T}}\boldsymbol{V}_J) \quad = \boldsymbol{Y}_J \\
\boldsymbol{N}_{\mathrm{Al\_a}J} & = \mathrm{dual}\,(\boldsymbol{X}'^{\mathrm{T}}\boldsymbol{V}_J) \\
\boldsymbol{N}_{\mathrm{Al\_l}J} & = \mathrm{primal}\,(\boldsymbol{X}'^{\mathrm{T}}\boldsymbol{V}_J) \quad = \boldsymbol{N}_{\mathrm{Aa\_a}J} \\
\hline
\boldsymbol{\mathcal{N}}_{\mathrm{Aa\_aa}JK} & = \mathrm{primal}\left(\boldsymbol{X}'^{\mathrm{T}}\boldsymbol{\mathcal{V}}_{JK} - \tfrac{1}{2}(\boldsymbol{I}^{\times}\boldsymbol{X}'^{\mathrm{T}}\boldsymbol{V}_J)^{\mathrm{T132}}\boldsymbol{X}'^{\mathrm{T}}\boldsymbol{V}_K\right) \quad = \boldsymbol{\mathcal{Y}}_{JK} - \tfrac{1}{2}(\boldsymbol{I}^{\times}\boldsymbol{Y}_J)^{\mathrm{T132}}\boldsymbol{Y}_K \\
\boldsymbol{\mathcal{N}}_{\mathrm{Al\_aa}JK} & = \tfrac{1}{2}\,\mathrm{dual}\left(\boldsymbol{X}'^{\mathrm{T}}\boldsymbol{\mathcal{V}}_{JK} - (\boldsymbol{I}^{\times}\boldsymbol{X}'^{\mathrm{T}}\boldsymbol{V}_J)^{\mathrm{T132}}\boldsymbol{Y}_K + \left(\boldsymbol{X}'^{\mathrm{T}}\boldsymbol{\mathcal{V}}_{KJ} - (\boldsymbol{I}^{\times}\boldsymbol{X}'^{\mathrm{T}}\boldsymbol{V}_K)^{\mathrm{T132}}\boldsymbol{Y}_J\right)^{\mathrm{T132}}\right) \quad = \boldsymbol{\mathcal{N}}_{\mathrm{Al\_aa}KJ}^{\mathrm{T132}} \\
\boldsymbol{\mathcal{N}}_{\mathrm{Al\_la}JK} & = \mathrm{primal}\left(\boldsymbol{X}'^{\mathrm{T}}\boldsymbol{\mathcal{V}}_{JK} - \tfrac{1}{2}(\boldsymbol{I}^{\times}\boldsymbol{X}'^{\mathrm{T}}\boldsymbol{V}_J)^{\mathrm{T132}}\boldsymbol{X}'^{\mathrm{T}}\boldsymbol{V}_K\right) \quad = \boldsymbol{\mathcal{N}}_{\mathrm{Aa\_aa}JK} \\
\boldsymbol{\mathcal{N}}_{\mathrm{Al\_al}JK} & = \mathrm{primal}\left(\boldsymbol{X}'^{\mathrm{T}}\boldsymbol{\mathcal{V}}_{KJ} - \tfrac{1}{2}(\boldsymbol{I}^{\times}\boldsymbol{X}'^{\mathrm{T}}\boldsymbol{V}_K)^{\mathrm{T132}}\boldsymbol{X}'^{\mathrm{T}}\boldsymbol{V}_J\right)^{\mathrm{T132}} \quad = \boldsymbol{\mathcal{N}}_{\mathrm{Al\_la}KJ}^{\mathrm{T132}} \\
\hline
\boldsymbol{\mathcal{N}}_{\mathrm{Ka\_a}J} & = \mathrm{primal}\left(\boldsymbol{X}'^{\mathrm{T}}(\boldsymbol{\mathcal{W}}_{Ji} + \tfrac{1}{2}\boldsymbol{k}'_i\times\boldsymbol{V}_J)\right)\otimes\boldsymbol{g}^i \quad = (\boldsymbol{\mathcal{Z}}_{Ji} + \tfrac{1}{2}\boldsymbol{k}'_{ai}\times\boldsymbol{Y}_J)\otimes\boldsymbol{g}^i \\
\boldsymbol{\mathcal{N}}_{\mathrm{Kl\_a}J} & = \mathrm{dual}\left(\boldsymbol{X}'^{\mathrm{T}}(\boldsymbol{\mathcal{W}}_{Ji} + \tfrac{1}{2}\boldsymbol{k}'_i\times\boldsymbol{V}_J)\right)\otimes\boldsymbol{g}^i \\
\boldsymbol{\mathcal{N}}_{\mathrm{Kl\_l}J} & = \mathrm{primal}\left(\boldsymbol{X}'^{\mathrm{T}}(\boldsymbol{\mathcal{W}}_{Ji} + \tfrac{1}{2}\boldsymbol{k}'_i\times\boldsymbol{V}_J)\right)\otimes\boldsymbol{g}^i \quad = \boldsymbol{\mathcal{N}}_{\mathrm{Ka\_a}J} \\
\hline
\mathbb{N}_{\mathrm{Ka\_aa}JK} & = \mathrm{primal}\left(\boldsymbol{X}'^{\mathrm{T}}\left(\mathbb{W}_{JKi} + \tfrac{1}{2}\boldsymbol{k}'_i\times\boldsymbol{\mathcal{V}}_{JK} + \tfrac{1}{2}(\boldsymbol{I}^{\times}\boldsymbol{\mathcal{W}}_{Ji})^{\mathrm{T132}}\boldsymbol{V}_K + \tfrac{1}{2}((\boldsymbol{I}^{\times}\boldsymbol{\mathcal{W}}_{Ki})^{\mathrm{T132}}\boldsymbol{V}_J)^{\mathrm{T132}} + ((\boldsymbol{I}\otimes\boldsymbol{k}'_i)^{\underline{\mathrm{S123}}}\boldsymbol{V}_J)^{\mathrm{T132}}\boldsymbol{V}_K\right)\right)\otimes\boldsymbol{g}^i \\
\mathbb{N}_{\mathrm{Kl\_aa}JK} & = \mathrm{dual}\left(\boldsymbol{X}'^{\mathrm{T}}\left(\mathbb{W}_{JKi} + \tfrac{1}{2}\boldsymbol{k}'_i\times\boldsymbol{\mathcal{V}}_{JK} + \tfrac{1}{2}(\boldsymbol{I}^{\times}\boldsymbol{\mathcal{W}}_{Ji})^{\mathrm{T132}}\boldsymbol{V}_K + \tfrac{1}{2}((\boldsymbol{I}^{\times}\boldsymbol{\mathcal{W}}_{Ki})^{\mathrm{T132}}\boldsymbol{V}_J)^{\mathrm{T132}} + ((\boldsymbol{I}\otimes\boldsymbol{k}'_i)^{\underline{\mathrm{S123}}}\boldsymbol{V}_J)^{\mathrm{T132}}\boldsymbol{V}_K\right)\right)\otimes\boldsymbol{g}^i \\
\mathbb{N}_{\mathrm{Kl\_la}JK} & = \mathrm{primal}\left(\boldsymbol{X}'^{\mathrm{T}}\left(\mathbb{W}_{JKi} + \tfrac{1}{2}\boldsymbol{k}'_i\times\boldsymbol{\mathcal{V}}_{JK} + \tfrac{1}{2}(\boldsymbol{I}^{\times}\boldsymbol{\mathcal{W}}_{Ji})^{\mathrm{T132}}\boldsymbol{V}_K + \tfrac{1}{2}((\boldsymbol{I}^{\times}\boldsymbol{\mathcal{W}}_{Ki})^{\mathrm{T132}}\boldsymbol{V}_J)^{\mathrm{T132}} + ((\boldsymbol{I}\otimes\boldsymbol{k}'_i)^{\underline{\mathrm{S123}}}\boldsymbol{V}_J)^{\mathrm{T132}}\boldsymbol{V}_K\right)\right)\otimes\boldsymbol{g}^i \quad = \mathbb{N}_{\mathrm{Ka\_aa}JK} \\
\mathbb{N}_{\mathrm{Kl\_al}JK} & = \mathrm{primal}\left(\boldsymbol{X}'^{\mathrm{T}}\left(\mathbb{W}_{JKi} + \tfrac{1}{2}\boldsymbol{k}'_i\times\boldsymbol{\mathcal{V}}_{JK} + \tfrac{1}{2}(\boldsymbol{I}^{\times}\boldsymbol{\mathcal{W}}_{Ji})^{\mathrm{T132}}\boldsymbol{V}_K + \tfrac{1}{2}((\boldsymbol{I}^{\times}\boldsymbol{\mathcal{W}}_{Ki})^{\mathrm{T132}}\boldsymbol{V}_J)^{\mathrm{T132}} + ((\boldsymbol{I}\otimes\boldsymbol{k}'_i)^{\underline{\mathrm{S123}}}\boldsymbol{V}_J)^{\mathrm{T132}}\boldsymbol{V}_K\right)\right)\otimes\boldsymbol{g}^i \quad = \mathbb{N}_{\mathrm{Kl\_la}KJ}^{\mathrm{T1324}}
\end{array}
$$

Box 3. Coefficient tensors of the derivative kinematical interpolation formulae.

The function-value columns and the tangent matrices were elaborated by Merlini and Morandini (2004b):

$$
\left\{\begin{array}{c}\boldsymbol{F}^V_{\mathrm{a}J}\\ \boldsymbol{F}^V_{\mathrm{l}J}\end{array}\right\} = \int_{V^e}\left(\left\{\begin{array}{c}\boldsymbol{\mathcal{N}}^{\mathrm{T213}}_{K\mathrm{l\_a}J} : \tilde{\boldsymbol{T}}\\ \boldsymbol{\mathcal{N}}^{\mathrm{T213}}_{K\mathrm{l\_l}J} : \tilde{\boldsymbol{T}}\end{array}\right\} - \left\{\begin{array}{c}\boldsymbol{N}^{\mathrm{T21}}_{\mathrm{Aa\_a}J}\cdot\boldsymbol{c} + \boldsymbol{N}^{\mathrm{T21}}_{\mathrm{Al\_a}J}\cdot\boldsymbol{f}\\ \boldsymbol{N}^{\mathrm{T21}}_{\mathrm{Al\_l}J}\cdot\boldsymbol{f}\end{array}\right\}\right)\mathrm{d}V^e
$$

$$
\boldsymbol{F}^V_{\tau J} = \int_{V^e}\boldsymbol{\Sigma}^{\mathrm{T}}_J\boldsymbol{I}^{\times} : \boldsymbol{\Phi}^{\mathrm{T}}\,\mathrm{dual}(\boldsymbol{X}'^{\mathrm{T}}\boldsymbol{\omega})\,\mathrm{d}V^e
$$

$$
\left[\begin{array}{cc}\boldsymbol{K}^V_{E\mathrm{aa}JK} & \boldsymbol{K}^V_{E\mathrm{al}JK}\\ \boldsymbol{K}^V_{E\mathrm{la}JK} & \boldsymbol{K}^V_{E\mathrm{ll}JK}\end{array}\right] = \int_{V^e}\left[\begin{array}{cc}\boldsymbol{\mathcal{N}}^{\mathrm{T213}}_{K\mathrm{l\_a}J} : \boldsymbol{\Phi}\mathbb{E}_{\varepsilon\mathrm{S}\varepsilon\mathrm{S}}\boldsymbol{\Phi}^{\mathrm{T}} : \boldsymbol{\mathcal{N}}^{\mathrm{T312}}_{K\mathrm{l\_a}K} & \boldsymbol{\mathcal{N}}^{\mathrm{T213}}_{K\mathrm{l\_a}J} : \boldsymbol{\Phi}\mathbb{E}_{\varepsilon\mathrm{S}\varepsilon\mathrm{S}\varepsilon\mathrm{S}}\boldsymbol{\Phi}^{\mathrm{T}} : \boldsymbol{\mathcal{N}}^{\mathrm{T312}}_{K\mathrm{l\_l}K}\\ \boldsymbol{\mathcal{N}}^{\mathrm{T213}}_{K\mathrm{l\_l}J} : \boldsymbol{\Phi}\mathbb{E}_{\varepsilon\mathrm{S}\varepsilon\mathrm{S}\varepsilon\mathrm{S}}\boldsymbol{\Phi}^{\mathrm{T}} : \boldsymbol{\mathcal{N}}^{\mathrm{T312}}_{K\mathrm{l\_a}K} & \boldsymbol{\mathcal{N}}^{\mathrm{T213}}_{K\mathrm{l\_l}J} : \boldsymbol{\Phi}\mathbb{E}_{\varepsilon\mathrm{S}\varepsilon\mathrm{S}\varepsilon\mathrm{S}}\boldsymbol{\Phi}^{\mathrm{T}} : \boldsymbol{\mathcal{N}}^{\mathrm{T312}}_{K\mathrm{l\_l}K}\end{array}\right]\mathrm{d}V^e
$$

$$
\left\{\begin{array}{c}\boldsymbol{K}^V_{K\mathrm{a}\tau JK}\\ \boldsymbol{K}^V_{K\mathrm{l}\tau JK}\end{array}\right\} = \int_{V^e}\left\{\begin{array}{c}\boldsymbol{\mathcal{N}}^{\mathrm{T213}}_{K\mathrm{l\_a}J} : \boldsymbol{\Phi}\boldsymbol{I}^{\times}\boldsymbol{\Sigma}_K\\ \boldsymbol{\mathcal{N}}^{\mathrm{T213}}_{K\mathrm{l\_l}J} : \boldsymbol{\Phi}\boldsymbol{I}^{\times}\boldsymbol{\Sigma}_K\end{array}\right\}\mathrm{d}V^e = \left[\begin{array}{cc}\boldsymbol{K}^{V^{\mathrm{T}}}_{K\tau\mathrm{a}KJ} & \boldsymbol{K}^{V^{\mathrm{T}}}_{K\tau\mathrm{l}KJ}\end{array}\right]^{\mathrm{T}} \tag{23}
$$

$$
\left[\begin{array}{cc}\boldsymbol{K}^V_{G\mathrm{aa}JK} & \boldsymbol{K}^V_{G\mathrm{al}JK}\\ \boldsymbol{K}^V_{G\mathrm{la}JK} & \boldsymbol{0}\end{array}\right] = \int_{V^e}\left(\left[\begin{array}{cc}\mathbb{N}^{\mathrm{T2143}}_{K\mathrm{l\_aa}JK}\vdots\tilde{\boldsymbol{T}}\otimes\boldsymbol{I} & \mathbb{N}^{\mathrm{T2143}}_{K\mathrm{l\_al}JK}\vdots\tilde{\boldsymbol{T}}\otimes\boldsymbol{I}\\ \mathbb{N}^{\mathrm{T2143}}_{K\mathrm{l\_la}JK}\vdots\tilde{\boldsymbol{T}}\otimes\boldsymbol{I} & \boldsymbol{0}\end{array}\right]\right.
$$

$$
\left.-\left[\begin{array}{cc}\boldsymbol{\mathcal{N}}^{\mathrm{T213}}_{\mathrm{Aa\_aa}JK} : \boldsymbol{c}\otimes\boldsymbol{I} + \boldsymbol{\mathcal{N}}^{\mathrm{T213}}_{\mathrm{Al\_aa}JK} : \boldsymbol{f}\ \otimes\boldsymbol{I} & \boldsymbol{\mathcal{N}}^{\mathrm{T213}}_{\mathrm{Al\_al}JK} : \boldsymbol{f}\ \otimes\boldsymbol{I}\\ \boldsymbol{\mathcal{N}}^{\mathrm{T213}}_{\mathrm{Al\_la}JK} : \boldsymbol{f}\ \otimes\boldsymbol{I} & \boldsymbol{0}\end{array}\right]\right)\mathrm{d}V^e
$$

and

$$\begin{aligned}
\begin{Bmatrix} \boldsymbol{F}^S_{\mathrm{a}J} \\ \boldsymbol{F}^S_{\mathrm{l}J} \end{Bmatrix} &= \int_{S^e_{\mathrm{f}}} \left(-\begin{Bmatrix} \boldsymbol{N}^{\mathrm{T21}}_{\mathrm{Al_a}J} \cdot (\boldsymbol{t} + \boldsymbol{\Phi}\boldsymbol{t}_{\mathrm{F}}) \\ \boldsymbol{N}^{\mathrm{T21}}_{\mathrm{Al_l}J} \cdot (\boldsymbol{t} + \boldsymbol{\Phi}\boldsymbol{t}_{\mathrm{F}}) \end{Bmatrix} \right) \mathrm{d}S^e_{\mathrm{f}} \\
\begin{bmatrix} \boldsymbol{K}^S_{G\mathrm{aa}JK} & \boldsymbol{K}^S_{G\mathrm{al}JK} \\ \boldsymbol{K}^S_{G\mathrm{la}JK} & \boldsymbol{0} \end{bmatrix} &= \int_{S^e_{\mathrm{f}}} \left(-\begin{bmatrix} \mathscr{N}^{\mathrm{T213}}_{\mathrm{Al_aa}JK} : (\boldsymbol{t} + \boldsymbol{\Phi}\boldsymbol{t}_{\mathrm{F}}) \otimes \boldsymbol{I} & \mathscr{N}^{\mathrm{T213}}_{\mathrm{Al_a}lJK} : (\boldsymbol{t} + \boldsymbol{\Phi}\boldsymbol{t}_{\mathrm{F}}) \otimes \boldsymbol{I} \\ \mathscr{N}^{\mathrm{T213}}_{\mathrm{Al_la}JK} : (\boldsymbol{t} + \boldsymbol{\Phi}\boldsymbol{t}_{\mathrm{F}}) \otimes \boldsymbol{I} & \boldsymbol{0} \end{bmatrix} \right. \\
&\qquad \left. + \begin{bmatrix} \boldsymbol{N}^{\mathrm{T21}}_{\mathrm{Al_a}J} \cdot (\boldsymbol{\Phi}\boldsymbol{t}_{\mathrm{F}}) \times \boldsymbol{N}_{\mathrm{Aa_a}K} & \boldsymbol{0} \\ \boldsymbol{N}^{\mathrm{T21}}_{\mathrm{Al_l}J} \cdot (\boldsymbol{\Phi}\boldsymbol{t}_{\mathrm{F}}) \times \boldsymbol{N}_{\mathrm{Aa_a}K} & \boldsymbol{0} \end{bmatrix} \right) \mathrm{d}S^e_{\mathrm{f}}.
\end{aligned} \tag{24}$$

It is worth noting that the tangent matrix turns out to be symmetrical, apart from the geometric stiffness related to volume couples and surface follower forces.

4.2. Resolution of the nodal mixed variation variables

When trying to assemble the tangent matrix of the discrete model, one has to face the unfamiliar problem of the mixed variation variables appearing in Eqs. $(21)_4$ and $(22)_2$: indeed, these mixed variation variables must be solved for the virtual and incremental variables separately before assembling the problem matrix. Once the problem matrix has been correctly assembled, the global virtual variables can be dropped, leaving the equations of the linearized problem, with the global incremental variables as unknowns. The resolution of the mixed variation variables is accomplished at each single node, where the kinematical variables are actually free variables.

From a Total Lagrangian standpoint, consider the rototranslations $\boldsymbol{H}_J$ that bring the nodal oriento-positions from $\boldsymbol{A}_J$ to $\boldsymbol{A}'_J = \boldsymbol{H}_J\boldsymbol{A}_J$ (see Part I, Section 4.5). The relevant exponential maps $\boldsymbol{H}_J = \exp(\boldsymbol{\eta}_J\times)$ and inverse logarithmic maps $\boldsymbol{\eta}_J \times = \log \boldsymbol{H}_J$ introduce the nodal helices $\boldsymbol{\eta}_J$ as actually free kinematical variables. The nodal differential oriento-position vectors $\boldsymbol{a}'_{\delta J}$, $\boldsymbol{a}'_{\partial J}$, $\boldsymbol{a}'_{\partial\delta J}$ coincide respectively with the nodal differential helices $\boldsymbol{\eta}_{\delta J}$, $\boldsymbol{\eta}_{\partial J}$, $\boldsymbol{\eta}_{\partial\delta J}$, which in turn are related to the variations of the nodal helices by the differential maps associated with the exponential map (see Part II, Appendix B). In particular, from Eq. $(\mathrm{B}\text{-}14)_2$ of Part II we have $\boldsymbol{\eta}_{\partial\delta J} = \boldsymbol{\Lambda}_J\partial\delta\boldsymbol{\eta}_J + \boldsymbol{\Lambda}^{1\underline{2}\underline{\underline{3}}}_{\mathrm{III}J} : \delta\boldsymbol{\eta}_J \otimes \partial\boldsymbol{\eta}_J$, where $\boldsymbol{\Lambda}_J$ and $\boldsymbol{\Lambda}^{1\underline{2}\underline{\underline{3}}}_{\mathrm{III}J}$ are the first and second differential mapping tensors associated with each nodal rototranslation $\boldsymbol{H}_J$, and are built with the current value of each nodal helix $\boldsymbol{\eta}_J$. Now, the double variations $\partial\delta\boldsymbol{\eta}_J$ of the free variables are obviously null (again, remember that the variational principle has been linearized with respect to the problem variables $\boldsymbol{\eta}_J$, not the independent and arbitrary variables $\delta\boldsymbol{\eta}_J$), and recalling Eqs. (B-15) and (B-17) from Part II we obtain $\boldsymbol{\eta}_{\partial\delta J} = \boldsymbol{\Lambda}_J\boldsymbol{\Lambda}^{-1\underline{2}\underline{\underline{3}}}_{\mathrm{III}J} : \boldsymbol{\eta}_{\delta J} \otimes \boldsymbol{\eta}_{\partial J}$. By turning back to the nodal differential oriento-position vectors, the resolution formula for the mixed variation variables follows:

$$\boldsymbol{a}'_{\partial\delta J} = \boldsymbol{\Lambda}_J\boldsymbol{\Lambda}^{-1\underline{2}\underline{\underline{3}}}_{\mathrm{III}J} : \boldsymbol{a}'_{\delta J} \otimes \boldsymbol{a}'_{\partial J}. \tag{25}$$

We remark that the resolution is local at each single node and nonlinearly dependent on the current value of the nodal oriento-position.

Using Eq. (25) in Eq. $(21)_4$, the geometric contribution $\partial\Pi^{Ve}_{\delta G}$ of the volume element takes the form

$$\partial\Pi^{Ve}_{\delta G} = \sum_{J=1}^{N}\sum_{K=1}^{N} \begin{Bmatrix} \boldsymbol{a}'_{\mathrm{a}\delta J} \\ \boldsymbol{a}'_{\mathrm{l}\delta J} \end{Bmatrix}^{\mathrm{T}} \cdot \left(\begin{bmatrix} \boldsymbol{K}^V_{F\mathrm{aa}JK} & \boldsymbol{K}^V_{F\mathrm{al}JK} \\ \boldsymbol{K}^V_{F\mathrm{la}JK} & \boldsymbol{0} \end{bmatrix} + \begin{bmatrix} \boldsymbol{K}^V_{G\mathrm{aa}JK} & \boldsymbol{K}^V_{G\mathrm{al}JK} \\ \boldsymbol{K}^V_{G\mathrm{la}JK} & \boldsymbol{0} \end{bmatrix} \right) \cdot \begin{Bmatrix} \boldsymbol{a}'_{\mathrm{a}\partial K} \\ \boldsymbol{a}'_{\mathrm{l}\partial K} \end{Bmatrix}, \tag{26}$$

where

$$\begin{bmatrix} \boldsymbol{K}^V_{F\mathrm{aa}JK} & \boldsymbol{K}^V_{F\mathrm{al}JK} \\ \boldsymbol{K}^V_{F\mathrm{la}JK} & \boldsymbol{0} \end{bmatrix} = \delta_{JK} \begin{bmatrix} \boldsymbol{F}^V_{\mathrm{a}J} \cdot \mathrm{primal}(\boldsymbol{\Lambda}_J\boldsymbol{\Lambda}^{-1\underline{2}\underline{\underline{3}}}_{\mathrm{III}J}) + \boldsymbol{F}^V_{\mathrm{l}J} \cdot \mathrm{dual}(\boldsymbol{\Lambda}_J\boldsymbol{\Lambda}^{-1\underline{2}\underline{\underline{3}}}_{\mathrm{III}J}) & \boldsymbol{F}^V_{\mathrm{l}J} \cdot \mathrm{dual}(\boldsymbol{\Lambda}_J\boldsymbol{\Lambda}^{-1\underline{2}\underline{\underline{3}}}_{\mathrm{III}J}) \\ \boldsymbol{F}^V_{\mathrm{l}J} \cdot \mathrm{dual}(\boldsymbol{\Lambda}_J\boldsymbol{\Lambda}^{-1\underline{2}\underline{\underline{3}}}_{\mathrm{III}J}) & \boldsymbol{0} \end{bmatrix} \tag{27}$$

is a new symmetric and 'lumped' contribution to the geometric stiffness matrix. The same considerations apply to the geometric contribution $\partial \Pi^{S_f^e}_{\delta G}$ of the surface element in Eq. $(22)_2$.

4.3. Methodology of analysis

In a nonlinear boundary value problem, the equations from the approximated variational principle are solved iteratively. At a given configuration during the iterative process, the integrands of the element matrices in Eqs. (23) and (24) are evaluated at each quadrature point as discussed next. The oriento-position $\boldsymbol{A}' = \boldsymbol{X}'\boldsymbol{\alpha}' = (\boldsymbol{I} + \varepsilon \boldsymbol{x}'\times)\boldsymbol{\alpha}'$ is interpolated among the nodal oriento-positions $\boldsymbol{A}'_J$ by the multiplicative scheme presented in Part II. The interpolation algorithm also provides the curvature $\boldsymbol{k}' = \boldsymbol{A}'\mathrm{ax}(\boldsymbol{A}'^{\mathrm{T}}\boldsymbol{A}'_{/\otimes})$ that characterizes the oriento-position gradient, and the coefficient tensors $\boldsymbol{V}_J$, $\mathscr{V}_{JK}$, $\mathscr{W}_J$, $\mathbb{W}_{JK}$ (Eqs. (15) and (17) of Part II), from which the coefficient tensors of the derivative interpolation formulae as given in Box 3 are computed. Note that at the beginning of the analysis, the reference oriento-position $\boldsymbol{A} = \boldsymbol{X}\boldsymbol{\alpha} = (\boldsymbol{I} + \varepsilon \boldsymbol{x}\times)\boldsymbol{\alpha}$ and curvature $\boldsymbol{k} = \boldsymbol{A}\,\mathrm{ax}(\boldsymbol{A}^{\mathrm{T}}\boldsymbol{A}_{/\otimes})$ have been interpolated in exactly the same way among the initial nodal oriento-positions $\boldsymbol{A}_J$. Moreover, the reference base vectors $\boldsymbol{g}_i$ and $\boldsymbol{g}^i$ have been computed, as described in Part II, Section 4.4, in order to recover any current tensor by its dyadic form, consistently with a Total Lagrangian analysis scheme. Such reference quantities are made available throughout the whole nonlinear analysis. In particular, this allows the recovery of the rototranslation $\boldsymbol{H} = (\boldsymbol{I} + \varepsilon(\boldsymbol{x}' - \boldsymbol{\Phi}\boldsymbol{x})\times)\boldsymbol{\Phi}$ as $\boldsymbol{H} = \boldsymbol{A}'\boldsymbol{A}^{\mathrm{T}}$, and of the kinematical strain $\boldsymbol{\omega} = \boldsymbol{H}\,\mathrm{ax}(\boldsymbol{H}^{\mathrm{T}}\boldsymbol{H}_{/\otimes})$, that characterizes the rototranslation gradient, as $\boldsymbol{\omega} = \boldsymbol{k}' - \boldsymbol{H}\boldsymbol{k}$ (see Part I, Sections 4.5 and 4.6). The symmetric strain parameter is then computed as $\boldsymbol{\varepsilon}^{\mathrm{S}} = (\boldsymbol{\Phi}^{\mathrm{T}}\,\mathrm{dual}(\boldsymbol{X}'^{\mathrm{T}}\boldsymbol{\omega}))^{\mathrm{S}}$ and is used by the constitutive model of nonlinear elasticity to compute the Biot-stress symmetric part $\hat{\boldsymbol{T}}^{\mathrm{S}}$ and its tangent map, the elastic tensor $\mathbb{E}_{\varepsilon^{\mathrm{S}}\varepsilon^{\mathrm{S}}}$. The Biot-axial $\hat{\boldsymbol{\tau}}$ is interpolated among the discrete Biot-axials $\hat{\boldsymbol{\tau}}_J$ as in Eq. (17), and the first Piola–Kirchhoff stress is recovered as $\tilde{\boldsymbol{T}} = \boldsymbol{\Phi}\hat{\boldsymbol{T}} = \boldsymbol{\Phi}(\hat{\boldsymbol{T}}^{\mathrm{S}} + \hat{\boldsymbol{\tau}}\times)$. In a stepwise loading history, the external load densities $\boldsymbol{f}$, $\boldsymbol{c}$, $\boldsymbol{t}$ and $\boldsymbol{t}_{\mathrm{F}}$ are that fraction of the final analysis loads pertinent to the current step.

It is worth stressing that this approach is quite different from the analysis scheme usually adopted when the unknowns pertain to the Euclidean vector space, and adhered to as well when a rotation unknown is included in the context of classical modeling. In our scheme, we carefully avoid the interpolation of the rototranslation field among the nodal rototranslations. Instead, we interpolate the oriento-position field and obtain the curvature over the element domain, in a consistent manner for both the reference configuration and any current configuration. The local rototranslation is recovered by comparing the oriento-positions in the current and reference configurations, and the kinematical strain is computed by comparing the curvatures. This approach leads to a path-independent finite-element analysis.

At each load step, the linearized principle $\Pi_\delta + \partial\Pi_\delta = 0$ is solved numerically by an iterative procedure of the Newton–Raphson kind. At each iteration, the linear equation set is solved for the incremental variables $\boldsymbol{a}'_{\partial J}$ (which coincide with the nodal incremental helices $\boldsymbol{\eta}_{\partial J}$) and $\partial\hat{\boldsymbol{\tau}}_J$. Consistently with the concept of helicoidal modeling, the unknown nodal oriento-positions are updated multiplicatively according to the formula

$$\boldsymbol{A}'_J \leftarrow \exp(\boldsymbol{\eta}_{\partial J}\times)\boldsymbol{A}'_J, \tag{28}$$

while the unknown discrete Biot-axials are updated additively, $\hat{\boldsymbol{\tau}}_J \leftarrow \hat{\boldsymbol{\tau}}_J + \partial\hat{\boldsymbol{\tau}}_J$.

It can be observed that the discrete kinematical incremental unknowns $\boldsymbol{a}'_{\partial J}$ are pole-based dual vectors, whose linear parts $\boldsymbol{a}'_{\mathrm{l}\partial J} = \boldsymbol{\alpha}'_J\partial(\boldsymbol{\alpha}'^{\mathrm{T}}_J\boldsymbol{x}'_J)$ (recall Eq. (40) of Part I) are dependent on the choice of the pole and are finitely affected by the magnitude of the position vectors (in the present formulation, the pole is chosen coincident with the origin for convenience). For numerical reasons, when position vectors are large, it can be preferable to change the problem unknowns just for the solution time and accordingly transform the function-value column and tangent matrix of the finite-element model. The change of unknowns can be performed node-by-node using the position tensors $\boldsymbol{X}'_J$ reached in the current configuration, and so it

corresponds to self-basing the nodal virtual and incremental variables from $\boldsymbol{a}'_{\delta J}$ to $\boldsymbol{X}'^{\mathrm{T}}_J \boldsymbol{a}'_{\delta J}$ and from $\boldsymbol{a}'_{\partial J}$ to $\boldsymbol{X}'^{\mathrm{T}}_J \boldsymbol{a}'_{\partial J}$, just before solving the linear equation set. Then, the inverse transformation is applied to the computed solution, and the origin-based nodal incremental variables $\boldsymbol{a}'_{\partial J}$ are recovered before updating the nodal oriento-positions. In the computational procedure, this 'self-basing' process of the problem unknowns is left as an option. It proves a useful tool to lower the numerical conditioning of the coefficient matrix and to relieve any numerically induced dependency of the solution on the choice of the pole.

This computational feature offers another convenient advantage: it also provides the means of uncoupling the incremental positions from the incremental orientations. In fact, the angular and linear parts of the self-based dual vectors $\boldsymbol{X}'^{\mathrm{T}}_J \boldsymbol{a}'_{\partial J}$ are just the incremental rotation vectors $\boldsymbol{\varphi}_{\partial J}$ and the incremental positions $\partial \boldsymbol{x}'_J$, respectively (see Eq. (41) of Part I). As such, the 'self-basing' option can be profitably exploited to model selective external constraints, i.e. constraints on a subset of the degrees-of-freedom of a node. While waiting for suitable constraint elements, in the test cases we will discuss below, the rigid body motion has been grounded simply by temporarily removing the appropriate incremental unknowns from the equation set.

5. Element design

5.1. Geometry and shape functions

We developed elements defined over rectangular domains, precisely a hexahedral element to model the body volume and a quadrilateral element to model the surface loads. The edges of such elements lie along material coordinate lines, which are restricted to the range $\xi^i = [-1, +1]$. In the present work, we consider low-order elements equipped with only corner nodes; they exploit standard multilinear weight functions,

$$W_J = \frac{1}{N} \prod_{i=1}^{n} (1 + \xi^i \xi^i_J), \quad (J = 1, 2, \ldots N), \tag{29}$$

with n the number of coordinates ($n = 3$ for the volume element and $n = 2$ for the surface element) and $N = 2^n$ the number of nodes. Note that the helicoidal interpolation of the oriento-position (Part II) over the element faces and along the element edges allows for curved geometries also in the undeformed configuration, so the proposed elements are a generally curved hexahedron and a generally space-curved quadrilateral. We refer to such elements as *helicoidal elements*.

It is worth noting that, using the multiplicative interpolation proposed in Part II and the weight functions in Eq. (29), the evaluation of the substitute kinematical field on a face (or edge) depends only on the corner nodes relevant to that face (or edge). This means that the oriento-positions on a face (or edge) are shared by two adjacent elements, so that the proposed elements are C^0-continuous both for the orientations and for the positions.

5.2. Substitute Biot-axial field

A major difficulty encountered in the design of the volume element was the formulation of the substitute field of the Biot-axial variable against the helicoidal substitute field of the kinematical variables, and therefore the choice of the discrete Biot-axial parameters. The issue concerns the role of the Biot-axial variable in the formulation of the non-polar medium. According to Eq. $(9)_1$, the virtual axial vector of the Biot stress acts as the Lagrange multiplier of the kinematical constraint, Eq. (6), which actually defines the rotation of

the medium. Now, in the context of classical modeling, the position and orientation fields are uncoupled: the displacement determines a deformation gradient (hence strains and elastically induced stresses), and on the other hand the rotation freedom can be directly withstood by a workless Biot-axial field. In the helicoidal modeling, instead, the orientation is part of a unique oriento-position dual field, so the rotation appears to be co-responsible for strains, thus it seems in principle susceptible to be withstood by an elastically induced stress field. So, the issue is to understand how the substitute Biot-axial field is working over the helicoidal element domain, and this is not an easy task.

In our past finite element formulation (Merlini, 1997), we were adhering to a classical modeling and we resorted to approximations of the Biot-axial and rotation vector fields consistent with each other. In particular, we took both fields as internal variables, constant within the element, thus discontinuous across adjacent elements. At that time, such choice circumvented the difficulty of interpolating rotations and led to a finite element of satisfactory performance in geometrically nonlinear problems, in spite of the coarse representation of the rotation field, and, at the same time, avoided the regularization of the variational principle (see Hughes and Brezzi, 1989). In the present case of helicoidal modeling, an attempt to use a constant Biot-axial field was unsuccessful. The intrinsic rotational lability arising from an inadequate quantity of Biot-axial unknowns had to be constrained by grounding the rotational d.o.f.'s somewhere in the model; however, the element performs rather well in some circumstances (e.g. bending), but badly in others (twisting).

An insight came from the eigenvalue analysis of the matrix of an unstressed cubic element. We investigated three cases. First, a free element is considered (48 kinematical d.o.f.'s). In the absence of Biot-axial unknowns, 12 null eigenvalues out of 48 are found (six more than the rigid body freedoms); by adding a constant Biot-axial vector field, the null eigenvalues reduce to 9 out of 51. In the second case, using the 'self-basing' option discussed earlier, the positions of the eight corners are grounded, leaving an element with 24 rotational d.o.f.'s and without rigid body freedoms. With no Biot-axial field, 6 null eigenvalues out of 24 are found in this case, and they reduce to 3 out of 27 with a constant Biot-axial field. In the last case, 16 more d.o.f.'s are constrained, leaving exactly one drilling rotational freedom at each node. Rotations are all planar in this case, and the null eigenvalues reduce to 2 out of 8 with no Biot-axial field, and to 1 out of 9 with a constant Biot-axial field. The eigenvectors with null eigenvalue with no Biot-axial field are shown in Fig. 1, and result in a combination of a mode of constant rotation over the whole element and a mode of skew drilling rotation. Now, it is clear that, in addition to the rank deficiency of rigid motion, the stiffness matrix without the Biot-axial restraint is *six* times singular due to the rotation field, and the true role of the substitute Biot-axial field becomes that of withstanding such rotational modes. A constant Biot-axial field is able to withstand the constant-rotation mode, so relieving the primary intrinsic rotational lability, but it cannot withstand the skewing-rotation mode and leaves three spurious twisting modes around the coordinate lines.

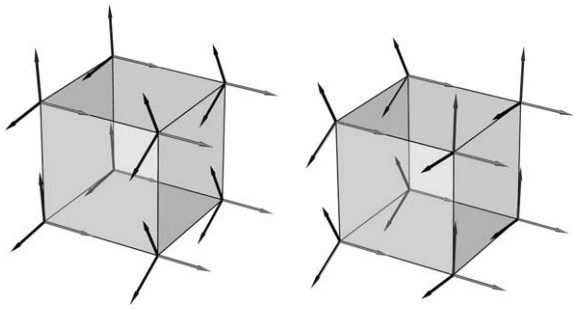

Fig. 1. Spurious drilling modes of the volume element without Biot-axial field.

Following this analysis, we devised a three-linear interpolation scheme of the Biot-axial vector between the opposite faces of the hexahedron. A single Biot-axial component is associated with each face, so the Biot-axial field is determined by exactly *six* unknowns. Each scalar unknown is multiplied by the unit normal at the face centroid to form a Biot-axial vector normal to the face. If we number the faces using a pair of indexes iJ ($i = 1,2,3$; $J = 1,2$) that identify respectively a coordinate ξ^i and which face is crossed by that coordinate, the interpolation formula writes

$$\hat{\boldsymbol{\tau}} = \sum_{i=1}^{3} \sum_{J=1}^{2} W_{iJ} \boldsymbol{v}_{iJ} \hat{\tau}_{iJ}, \tag{30}$$

where the weight functions W_{iJ} are given by Eq. (29) with $n = 1$ and $N = 2$, $\boldsymbol{v}_{iJ}$ are the unit vectors normal to the face and $\hat{\tau}_{iJ}$ the relevant Biot-axial components. Eq. (30) can be easily brought to the form of Eq. (17) by substituting an ordered set of the discrete scalar variables $\hat{\tau}_{iJ}$ at the $F = 6$ faces for the discrete Biot-axial vectors $\hat{\boldsymbol{\tau}}_J$, and vectors of the form $\frac{1}{2}(1 \pm \xi^i)\boldsymbol{v}_{iJ}$ (i not summed) for tensors $\boldsymbol{\Sigma}_J$. In the finite-element model, the scalars $\hat{\tau}_{iJ}$ are part of the discrete set of the global Biot-axial variables. They are shared by the adjacent elements, so the substitute Biot-axial field is virtually continuous as for the components normal to the faces (it is actually continuous with rectangular meshes). It is also worth noting that a non-null Biot-axial vector $\hat{\boldsymbol{\tau}}_J = \boldsymbol{v}_J \hat{\tau}_J$ at a boundary face does not violate the balance equation $\boldsymbol{\Phi}\hat{\boldsymbol{T}}\boldsymbol{v} = \boldsymbol{0}$ on a free surface with no traction. The proposed interpolation scheme for the Biot-axial vector proves capable of completely removing any rotational lability and the null eigenvalues of the element matrix reduce to the expected 6 out of 54.

5.3. Three-dimensional elements

The volume element is an *8-nodes/6-faces hexahedron*, based on 48 kinematical unknowns and on 6 Biot-axial unknowns. The companion surface element, which is intended to model surface loads, is a *4-nodes quadrilateral* based on 24 kinematical unknowns. Note that both such helicoidal elements allow external loads: the body force and couple densities $\boldsymbol{f}$ and $\boldsymbol{c}$, and the surface traction densities $\boldsymbol{t}$ and $\boldsymbol{t}_{\mathrm{F}}$, are conveniently defined at the integration points of the relevant elements. The numerical integration over the element domain is performed by means of the Gauss quadrature rule with three integration points per coordinate (see discussion below).

5.4. Planar elements

Planar models can be analyzed by the same formulation by simply removing the appropriate out-of-plane unknown components. After forcing the metric to be planar, the volume and surface integrals reduce to area and line integrals. The constitutive models are properly fitted to deal with either plane-strain or plane-stress problems. The volume and surface elements reduce to the relevant two-dimensional counterparts, which are curved quadrilaterals and curved lines on a plane; they will be referred to as planar volume and planar surface elements, respectively.

Rototranslations are planar in this case, and rotations belong to a scalar field. Correspondingly, the Biot-axial field reduces to the scalar field of the out-of-plane component. In order to understand the proper Biot-axial interpolation for the planar case, an eigenvalue analysis has been performed on a planar volume element after grounding the corner positions. In absence of a Biot-axial field, the quadrilateral with just 4 drilling d.o.f.'s has a null eigenvalue corresponding to a spurious constant-rotation mode, and a constant Biot-axial field is able to relieve this rotational lability. A constant Biot-axial field does match the interpolation scheme discussed above for the three-dimensional case, as the element faces reduce to the only quadrilateral surface in the planar case.

The planar volume element is a *4-nodes/1-face quadrilateral* (12 kinematical unknowns and 1 Biot-axial unknown), and the planar surface element is a *2-nodes line* (6 kinematical unknowns).

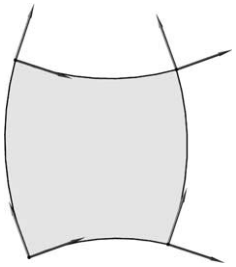

Fig. 2. Spurious mode of the planar volume element with 2×2 Gauss quadrature.

The eigenvalue analysis was also helpful to establish the proper integration rule for the proposed elements. A Gauss quadrature with two points per coordinate yields a singular stiffness matrix that gives spurious zero-energy modes (Fig. 2) similar to those observed in under-integrated elements with common quadratic shape functions (e.g. Hughes, 1987, Section 4.6). Three Gauss points per coordinate prove sufficient to avoid this rank deficiency and give a satisfactory performance in most test computations.

6. Examples with linear elastic material

The numerical tests we present next are carried out with an object-oriented finite-element code developed by the authors in C++ language. An original library of geometrical objects allows to manipulate in a plain way nested and recursive data structures, such as the polyadic forms of high-order tensors. This has proved crucial in coding very complicated expressions, such as the interpolation formulae of Part II. Moreover, the powerful features of the programming language allow to easily manage the formalism of dual algebra in a way that is transparent to the formalism of tensor algebra.

According to the present variational formulation, we assume that the hyperelastic constitutive models are based on a strain-energy function of the *linear-strain* symmetric tensor $\boldsymbol{\varepsilon}^{\mathrm{S}}$, work-conjugate to the Biot-stress symmetric part $\hat{\boldsymbol{T}}^{\mathrm{S}}$. We refer to such a parameterization of the strain energy as the *Biot-type parameterization*, in order to distinguish it from the commonly used Green-type parameterization, based on the Green–Lagrange *quadratic-strain* tensor $\boldsymbol{e}^{\mathrm{S}} = \frac{1}{2}(\boldsymbol{F}^{\mathrm{T}}\boldsymbol{F} - \boldsymbol{I})$. In the examples of this section we adopt a linear constitutive law for isotropic materials, deriving from the strain-energy quadratic function

$$w(\boldsymbol{\varepsilon}^{\mathrm{S}}) = \frac{1}{2}\hat{\lambda}(\operatorname{tr}\boldsymbol{\varepsilon}^{\mathrm{S}})^2 + \hat{\mu}\operatorname{tr}(\boldsymbol{\varepsilon}^{\mathrm{S}})^2, \tag{31}$$

where $\hat{\lambda}$ and $\hat{\mu}$ are Lamé moduli proper of the Biot-type parameterization. It is worth noting that the form in Eq. (31) of the well-known De Saint Venant–Kirchhoff strain-energy function is actually different from the commonly used form $w(\boldsymbol{e}^{\mathrm{S}}) = \frac{1}{2}\lambda(\operatorname{tr}\boldsymbol{e}^{\mathrm{S}})^2 + \mu\operatorname{tr}(\boldsymbol{e}^{\mathrm{S}})^2$, where λ and μ are the classical Lamé moduli of the Green-type parameterization. In particular, the reader should observe that, owing to the nonlinear relation $\boldsymbol{e}^{\mathrm{S}} = \frac{1}{2}((\boldsymbol{I} + \boldsymbol{\varepsilon}^{\mathrm{S}})(\boldsymbol{I} + \boldsymbol{\varepsilon}^{\mathrm{S}}) - \boldsymbol{I})$ between the two kinds of strain parameters, when deformations cannot be regarded as infinitesimal, a linear constitutive law for the Biot-type parameterization implies a nonlinear constitutive law for the Green-type parameterization, and vice versa. Therefore, the constants $\hat{\lambda}$ and $\hat{\mu}$ in Eq. (31) may not coincide in general with the classical constants λ and μ used to define a linear constitutive law with respect to the Green-type parameterization. In the following examples, the material input data are given as an elastic modulus E and a Poisson coefficient v, from which the Lamé moduli are computed as $\hat{\lambda} = Ev/(1+v)(1-2v)$ and $\hat{\mu} = E/2(1+v)$.

The examples in this section deal with high geometrical nonlinearities of beams clamped at one end (see also Merlini and Morandini, 2004a). The beams are loaded at the free end, either by means of dedicated

volume elements to introduce tip couples or by means of surface elements to introduce tip forces. In spite of the unusual modeling of beams by solid elements, such benchmark tests allow to assess the performance of the helicoidal modeling in bending dominated problems with large displacements and rotations. The reader should appreciate that in the images we present, the rendered geometry is helicoidally interpolated from the corner oriento-positions just like the local oriento-positions are at the integration points.

The solution of an elastic problem with the present formulation comprises the Biot-axial field as a primary unknown field. Since we exploit isotropic materials in our examples, it is important to observe that in this case the Biot stress is generally symmetrical (cf. Bufler, 1985; Simo et al., 1992), apart from the regions where external body couples are present (see Section 3.1). So, in the following examples a non-null Biot-axial has to be expected only within the tip elements carrying body couples. Instead, in this approximate analysis where the field equations (equilibrium and kinematical constraint) are satisfied only in a weak sense, the discrete Biot-axial unknowns are generally non-null also far from the loaded extremities, although they remain much smaller than the working stresses. We will present some results in terms of the discrete Biot-axial field in few simple examples: nevertheless, they suffice to recognize the computational role the substitute Biot-axial field is playing in the proposed finite element, namely that of withstanding any skew drilling rotation modes.

6.1. Planar beam roll-up

The aim of this example is to compare the helicoidal modeling with a classical modeling endowed with rotational degrees-of-freedom. A slender membrane of length $l = 10$ and height $h = 1$ is clamped at one end and bent by a tip couple. This problem is analyzed in plane stress, assuming $E = 1200$ and $\nu = 0.3$. The beam rolls into a complete circle under a couple $M = \kappa 2\pi EJ/l$, where κ is a correction factor accounting for low aspect ratio l/h, which has been evaluated $\kappa = 0.9255$ for a 10×1 membrane (Merlini, 1997). A very coarse mesh is used (ten square elements plus a tip element carrying the volume couple), however a good performance in planar bending is attained. In Fig. 3, the undeformed mesh and the final configurations are shown as obtained by the present formulation and by the classical modeling, based on constant rotation and Biot-axial fields over the element (Merlini, 1997). Ibrahimbegović and Frey (1993, 1995) observed an even stiffer behavior using 4-node elements with interpolated rotations, and achieved satisfactory results by resorting to incompatible modes. The tip corner nodes $(10, -0.5)$ and $(10, 0.5)$ reach the final coordinates $(-1.445, 0.045)$ and $(-0.829, 0.806)$, respectively. The final Biot-axial scalar components are listed in Table 1. Within the appended tip element, the Biot-axial is withstanding the body couple valued $M = 58.153$, while in the other unloaded elements it shows an alternating decay starting from the beam tip; however, it remains smaller than the maximum axial stress by at least two orders of magnitude.

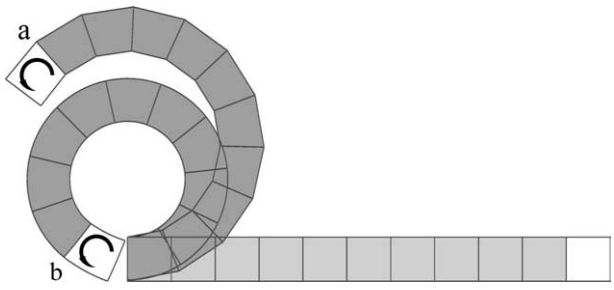

Fig. 3. Planar beam roll-up. Beam deformation by (a) classical modeling (Merlini, 1997) and (b) helicoidal modeling.

Table 1
Planar beam roll-up

Bay	$\hat{\tau}$
1	0.020
2	−0.027
3	0.045
4	−0.079
5	0.142
6	−0.258
7	0.471
8	−0.859
9	1.496
10	−2.091
Tip	−27.502

Biot-axial scalar field.

6.2. Cantilever beam

The examples in this section concern a three-dimensional cantilever beam of length $l = 10$, square cross-section 1×1 and properties $E = 1200$ and $\nu = 0.3$. The first load case is a bending tip couple as in the planar example. Since no correction factor is available for a three-dimensional case, the same value $\kappa = 0.9255$ as for the plane-stress analysis is assumed for the final couple to achieve a full circle. As shown in Fig. 4, the element has an excellent capacity of modeling constant-curvature geometries and of bending up to near π. In this load case, the deformation is almost insensitive to the mesh refinement along the beam axis, and the final average tip coordinates in the bending plane are respectively $(-0.947, 0.362)$ for mesh $1 \times 1 \times 2$, $(-1.062, 0.381)$ for mesh $1 \times 1 \times 5$, and $(-1.058, 0.374)$ for mesh $1 \times 1 \times 10$. The Biot-axial components normal to the bending plane are listed in Table 2, while the other components remain smaller by three orders of magnitude. These results look quite similar to those obtained in the planar case.

The convergence of the element can be assessed by refining the mesh on the beam cross-section. Six meshes of five bays were analyzed, respectively $1 \times 1 \times 5$, $2 \times 2 \times 5$, $3 \times 3 \times 5$, $4 \times 4 \times 5$, $6 \times 6 \times 5$ and $12 \times 12 \times 5$. As the element size diminishes, the circle closes, see Fig. 5 (where the performance of elements of very high aspect ratio is also worth noting) and Fig. 6. It is seen that the tip rotation of the finest mesh exceeds the expected 'exact' value of 2π, meaning that the right correction factor κ is actually smaller than for the planar case (Merlini, 1997). We attempted an estimate of the exact tip rotation in the present case by a parametric study of the trend of the error against the mesh refinement for several trial values, and we found that 2.0098π seems a fairly good measure. The log-plot of the error as based on this estimate evidences a quadratic rate of convergence (Fig. 7). This estimate corresponds to correcting the couple $2\pi EJ/l$ by a factor $\kappa = 0.921$ to achieve a tip rotation of 2π.

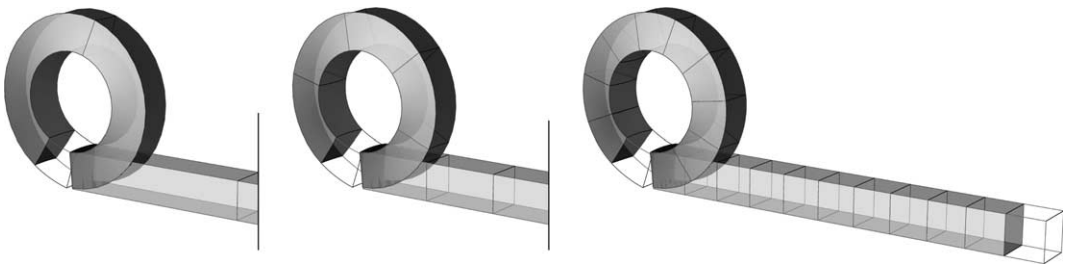

Fig. 4. Beam roll-up. Effect of the mesh refinement along the beam axis.

Table 2
Beam roll-up

Bay	$\hat{\tau}$		
	$1\times1\times2$	$1\times1\times5$	$1\times1\times10$
1		−0.246	0.018
2			−0.024
3	1.762	0.348	0.040
4			−0.072
5		−0.624	0.131
6			−0.241
7		1.235	0.443
8	−1.007		−0.819
9		−1.086	1.460
10			−2.071
Tip	−27.430	−27.288	−27.517

Biot-axial components normal to the bending plane.

The second load case ascertains the performance of the element in torsion. A torque is applied as a volume couple within the four tip elements appended to mesh $2\times2\times5$. The linear beam theory predicts a torque $M = KG\cdot\theta/l$ proportional to the tip rotation θ, with $K = 2.25/16$ the torsional moment of inertia in the case of a square cross-section 1×1 (e.g. Roark and Young, 1975). In the present analysis, the load is made to increase up to the value that corresponds to $\theta = 2\pi$ according to the linear formula. The torque/torsion response is almost linear in this case, and the stiffness we can measure with the coarse mesh used is about 0.8% greater than KG/l. Four helicoidal elements on the cross-section suffice to capture an approximate section warping, see Fig. 8. The Biot-axial unknowns at the model faces at 100% load are provided in Table 3. Also in this case, the Biot-axial field decays from the loaded tip and assumes values much smaller than 196, which is the maximum tangential stress under the applied torque.

The element sensitivity to irregular geometries is studied in the third load case, namely a transversal tip force. The reference mesh consists of $2\times2\times5$ prismatic elements. All the nodes at the clamped end are grounded, and four surface elements at the beam tip introduce the load as a distributed force. Next, two irregular meshes are derived (Fig. 9), that differ for the shape of the inner longitudinal edge between the four elements, which is a straight line in mesh (a) and a zigzag line in mesh (b). The tip positions in the bending plane under the final force $F = 10$ are listed in Table 4 and compared with the results obtained with two commercial codes (as tip position we mean the average position of the four tip-corner nodes). The values in Table 4 prove that the proposed helicoidal element is quite insensitive to mesh distortion, and to a greater extent than the elements ABAQUS C3D8I with incompatible modes and Marc 7 with assumed strains. The 20-nodes element ABAQUS C3D20R with reduced integration performs very well on both irregular meshes and could be assumed as a reference element for this test case. It must be noted that some of the irregular models show a certain amount of screwing and/or out-of-plane bending under the applied load. This is the case for all the models with ABAQUS C3D8I and Marc 7 elements and for model (b) with the helicoidal element (lateral tip deflection $Z = -0.260$), while this does not happen with the helicoidal element in mesh (a) and with the ABAQUS C3D20R element in any mesh.

6.3. L-shape cantilever

The problem of an elbow cantilever loaded by a transverse tip force is a good test for the interpolation scheme of the Biot-axial field. Two legs of length $l = 10$, square cross-section 1×1 and properties $E = 1200$ and $\nu = 0.3$, are clamped to each other at a right angle. The force $F = 1$ is distributed over a tip

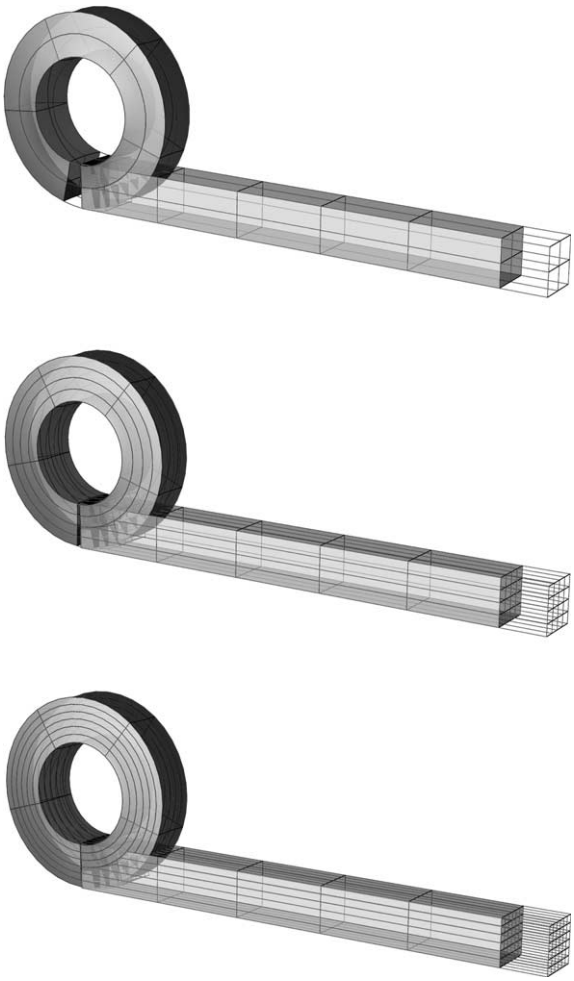

Fig. 5. Beam roll-up. Effect of the mesh refinement on the beam cross-section.

surface element, and the frame is analyzed with two coarse models of 7 and 6 elements respectively, which differ in the quoin (Fig. 10). The final average coordinates of the tip nodes (initially 10, 10, 0) are respectively (8.687, 5.835, −9.776) for the mesh with a cubic element at the corner, and (8.618, 5.934, −9.660) for the mesh with two trapezoidal elements. So, the two meshes provide a comparable kinematical response, even though the orientation of the faces that control the Biot-axial interpolation is quite different in the corner zone. In both meshes, significant values of the Biot-axial field are detected near the corner, from where they decay in an alternating fashion towards the leg extremities; however, the Biot-axial values at the faces are quite different for the two meshes (see Fig. 11), consistently with an expected different constraint mechanism of the rotational lability. In any case, the Biot-axial components remain smaller than the working stresses by almost two orders of magnitude (a ratio that is in general observed in all the computations performed).

6.4. Wrenched cantilever

Large three-dimensional rotations and distortions are experienced by a clamped beam wrenched by a tip force and a coaxial couple (see Merlini, 1997). The beam, of length $l = 25$, square cross-section 1×1 and

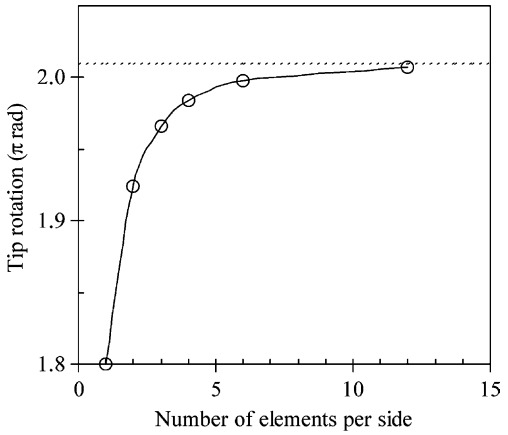

Fig. 6. Beam roll-up. Circle closing versus mesh refinement on the cross-section.

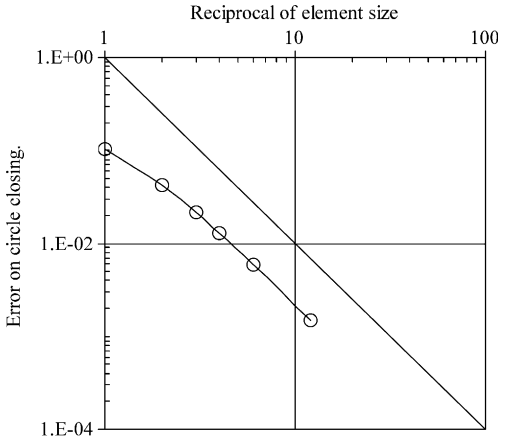

Fig. 7. Beam roll-up. Convergence rate with the element size assuming 2.0098π as exact value.

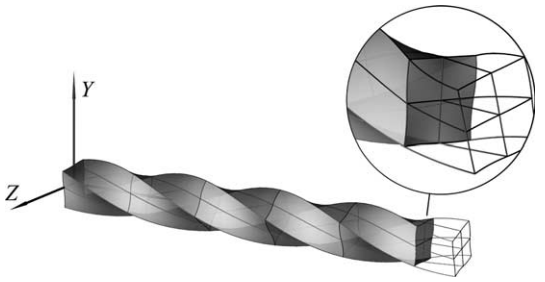

Fig. 8. Beam twist. Beam deformation with a tip rotation of 2π.

properties $E = 1200$ and $v = 0.3$, is coarsely modeled with $12 + 1$ elements. The force and couple are applied within the volume of the last cubic element and grow simultaneously up to the final values $F = 1.8$ and $M = 36$. This loading case is characterized by an abrupt change of configuration from about 40% to

Table 3
Beam twist

Bay	Transversal $\hat{\tau}$ at points with coordinates (Y,Z)			Longitudinal $\hat{\tau}$	Abscissa X
	$(-0.25,0.5)$	$(0.25,0.5)$	$(0,0.25)$		
				0.0898	0.0
1–2	1.2516	1.3007	1.5590		
				0.0021	0.2
3–4	−0.7705	2.4429	−0.5074		
				0.0899	0.4
5–6	3.8777	−1.7907	−0.7996		
				−0.4596	0.6
7–8	−0.6996	3.7667	0.6316		
				1.6225	0.8
9–10	3.9648	0.7238	−1.0586		
				−6.1289	1.0
Tip	−5.2343	0.3844	1.0855		
				−27.6716	1.1

Biot-axial components normal to the model faces.

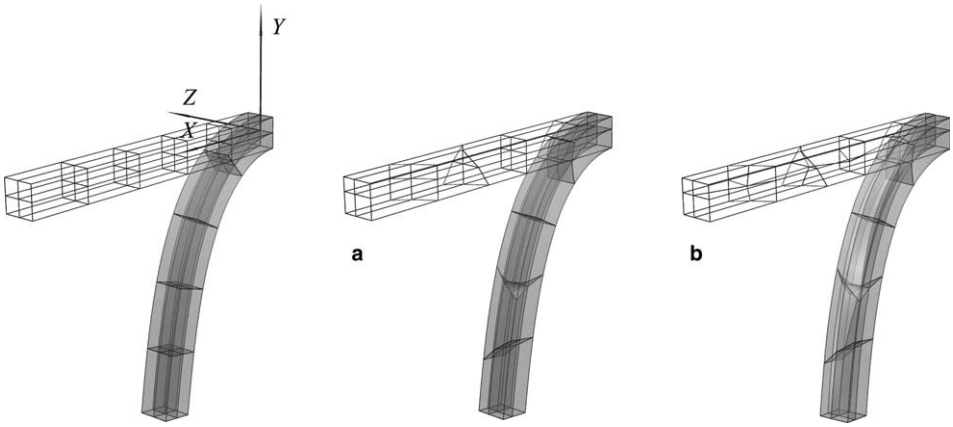

Fig. 9. Beam bending. Beam deformation with mesh $2\times2\times5$ and with two irregular meshes (a) and (b).

60% of the final load, in the course of which the force is observed to do a negative work (Fig. 12). The beam curls up to more than 450° and the average tip coordinates change from $(25,0,0)$ to $(2.798,4.392,1.672)$. This test case, if analyzed by a classical modeling with discontinuous rotation and Biot-axial fields, results much stiffer, cf. Merlini (1997).

The same cantilever was also analyzed by applying the force load after completion of the couple-load history. As a result of the first half-history, the beam rolls up to more than $5\pi/2$; then, under the transverse force, it screws more than $\pi/2$ and reaches exactly the same configuration as for the case of simultaneous loading (Fig. 13). The coordinates of the nodes of the tip element are listed in Table 5, where the figures of the last column are identical for the cases of simultaneous loading and of consecutive loading.

These computations are clear evidence of the path independence of the present analysis methodology. In addition, this example was exploited to verify the frame invariance of the proposed formulation: note that the properties of frame invariance and path independence of the interpolation scheme were discussed at length in Part II, Sections 2 and 3. The analysis was repeated on a model rigidly rototranslated by the dual

Table 4
Beam bending

	Mesh	X	Y
Helicoidal element	–	4.605	−8.066
	a	4.670	−7.993
	b	4.842	−7.951
ABAQUS C3D8I	–	4.847	−7.943
	a	5.918	−7.471
	b	6.059	−7.461
Marc 7 assumed strains	–	5.614	−7.491
	a	6.881	−6.833
	b	7.010	−6.747
ABAQUS C3D20R	–	4.442	−8.230
	a	4.507	−8.176
	b	4.511	−8.174

Final tip position in the bending plane.

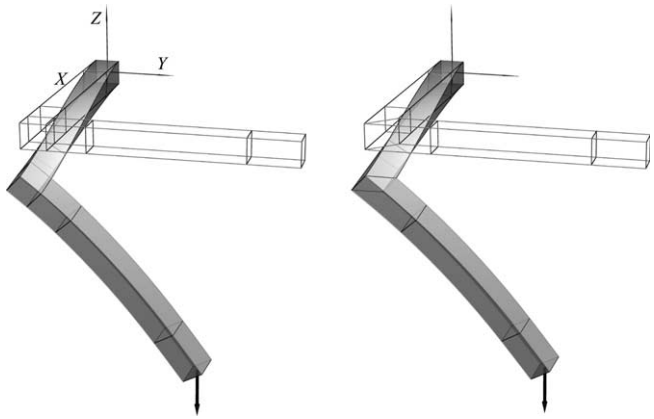

Fig. 10. L-shape cantilever. Frame deformation with two different meshes.

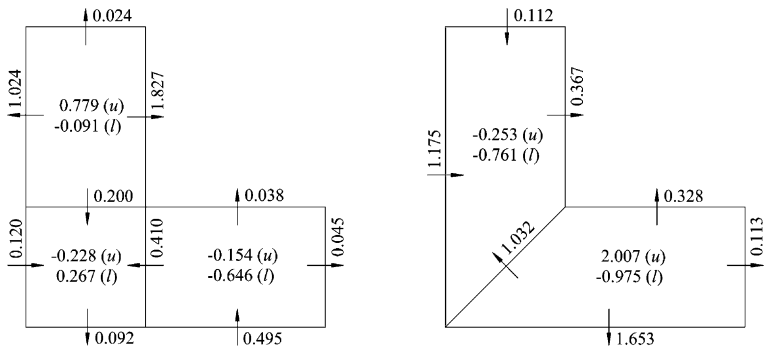

Fig. 11. L-shape cantilever. Biot-axial normal components in the corner zone for the two meshes. On the upper (u) and lower (l) surfaces the Biot-axial is positive upwards.

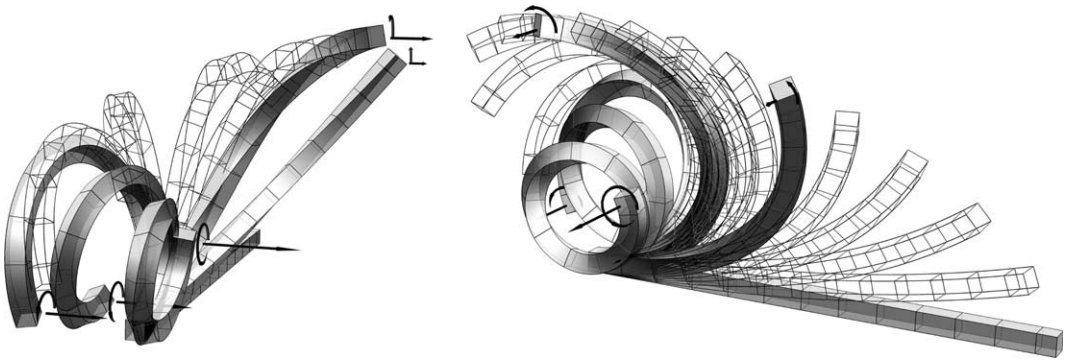

Fig. 12. Wrenched cantilever. Two views of the beam deformation every 20% of the load history (the intermediate configurations are drawn every 4% load).

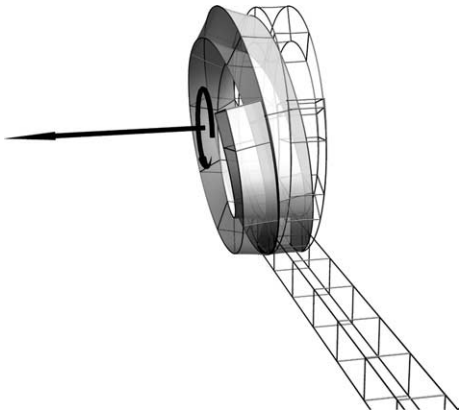

Fig. 13. Wrenched cantilever. Case of load history composed by first applying the tip couple alone, and subsequently superposing the tip force.

tensor $\boldsymbol{H} = (\boldsymbol{I} + \varepsilon \boldsymbol{t}\times)\exp(\boldsymbol{\varphi}\times)$, with translation vector $\boldsymbol{t} = 5\boldsymbol{i}^1 + 2\boldsymbol{i}^2 - 5\boldsymbol{i}^3$ and rotation vector $\boldsymbol{\varphi} = \frac{\pi}{\sqrt{69}}(\boldsymbol{i}^1 - 4\boldsymbol{i}^2 - 0.5\boldsymbol{i}^3)$. (The same rototranslation was used in the example discussed in Part II, which referred to the fourth element of this wrenched beam at 100% of simultaneous loading.) As expected, and in agreement with the kinematic analysis given in Part II, the loaded beam configurations are exactly the previous ones rototranslated by $\boldsymbol{H}$, and this confirms the frame invariance.

6.5. 45-degrees arc cantilever

The peculiarities of the last example of this section are a very slender body and an initially curved geometry. The curvilinear cantilever transversely loaded was proposed by Bathe and Bolourchi (1979) and used by several authors to test beam elements (see Ritto-Corrêa and Camotim (2002), Zupan and Saje (2003) and references therein) and also solid elements (Bathe and Bolourchi, 1979; Kožar and Ibrahimbegović, 1995; Moita and Crisfield, 1996; Klinkel and Wagner, 1997). The beam is a 45° arc of a circle of radius $R = 100$, square cross-section 1×1 and properties $E = 10^7$ and $v = 0$; it lies in the X–Y plane and the tip force $F = 600$ is directed along the Z-axis. We analyzed five meshes with respectively 1, 2, 4, 8 and 16 elements along the beam axis, plus a surface element at the arc tip carrying the load. The deformation of mesh

Table 5
Wrenched cantilever

		Undeformed	Under M alone	At 100% load
1	X	24.00	3.56675	2.52031
	Y	−0.50	3.56258	3.46759
	Z	−0.50	−0.47348	0.98938
2	X	24.00	2.58756	2.61029
	Y	0.50	3.41699	3.27919
	Z	−0.50	−0.52935	2.02565
3	X	24.00	2.58756	3.58431
	Y	0.50	3.41699	3.43038
	Z	0.50	0.52935	1.91221
4	X	24.00	3.56675	3.50230
	Y	−0.50	3.56258	3.59852
	Z	0.50	0.47348	0.98318
5	X	25.00	3.27443	2.25831
	Y	−0.50	4.61264	4.31631
	Z	−0.50	−0.48100	1.20210
6	X	25.00	2.32570	2.38966
	Y	0.50	4.29069	4.14899
	Z	−0.50	−0.51590	2.21093
7	X	25.00	2.32570	3.33123
	Y	0.50	4.29069	4.47276
	Z	0.50	0.51590	2.10830
8	X	25.00	3.27443	3.21085
	Y	−0.50	4.61264	4.63006
	Z	0.50	0.48100	1.16625

Positions of the nodes of the load-carrying tip element.

$1 \times 1 \times 4$ is shown in Fig. 14, and the final average tip coordinates are plotted in Fig. 15 against the number of elements. It can be seen that few elements (say 4) suffice to achieve a good accuracy, as the final tip position of the finest mesh is very close to the results from different solid-element formulations (Table 6).

6.6. Comments on the loading history

In spite of a satisfactory accuracy attained by the present formulation, the computational effectiveness is somewhat compromised by the high number of load steps necessary to complete the nonlinear analyses. Often, load increments smaller than those found elsewhere in literature are necessary. The computational burden in the examples of this section is evident from Table 7, where one can see that in several cases the initial step size could not be sustained and had to be halved. It is also noted that in general the step size must diminish with the mesh refinement. We are not yet able to give an explanation of the poor behavior of the present finite element modeling against load increments. However, an insight into this problem may come from the example of Section 8 below, after the discussion of a linear test case.

Within each load step, a fast convergence rate is observed, with an average of 5–6 iterations per step in most cases. As an example, the convergence rate for the last step of the 45° arc cantilever with a coarse mesh is provided in Table 8. Note that separate norms are computed for the angular, linear and Biot-axial unknowns of the problem. All the test cases were analyzed using the self-basing option discussed in Section

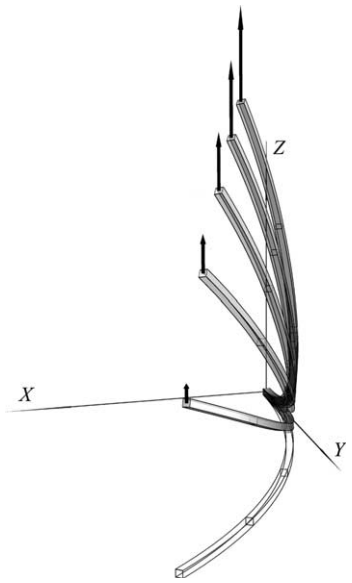

Fig. 14. 45° arc cantilever. Beam deformation every 20% of the load history.

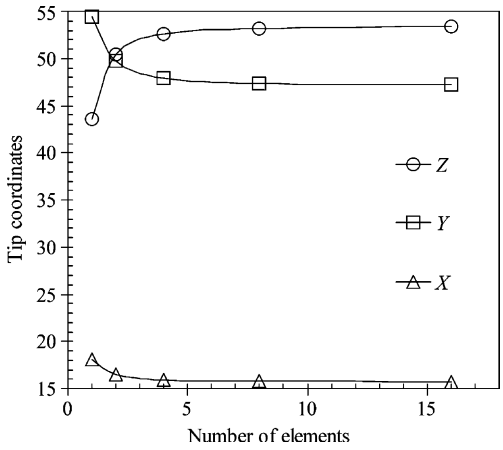

Fig. 15. 45° arc cantilever. Final tip position versus mesh refinement.

4.3, so the norms on the angular-part unknowns are representative of moments and rotations, and the norms on the linear-part unknowns are representative of forces and displacements.

The example of the wrenched cantilever under simultaneous loading was exploited instead to test the self-basing option discussed in Section 4.3. The same test case computed as a full pole-based analysis was completed in exactly the same number of total iterations as the self-based analysis (390). Moreover, the self-basing option does not deteriorate the convergence rate, as can be seen in the example of Table 9, where the figures that are identical for the two analyses are displayed only once. The effectiveness of the self-basing option was then tested by repeating both the self-based and pole-based analyses after giving an offset $(0, 0, 250)$ to the origin, i.e. the pole. We observed that the order of magnitude of the condition

Table 6
45° arc cantilever

	X	Y	Z
Bathe and Bolourchi (1979), also Moita and Crisfield (1996)	15.90	47.20	53.40
Kožar and Ibrahimbegović (1995)	15.65	47.41	53.21
Klinkel and Wagner (1997)	15.74	47.81	53.55
Present formulation	15.72	47.24	53.39

Final tip positions with different formulations using 16 solid elements.

Table 7
Solution history data for the examples with linear elastic material

Case		Load step initial size (%)	Number of load steps	Total number of iterations	Iterations per step		
					Min	Max	Average
Planar beam roll-up		5	21	121	4	7	5.76
Beam roll-up	$1\times1\times2$	5	23	136	5	9	5.91
	$1\times1\times5$	5	22	126	4	7	5.73
	$1\times1\times10$	5	22	133	5	10	6.05
	$2\times2\times5$	5	25	167	5	14	6.68
	$3\times3\times5$	5	31	179	5	8	5.77
	$4\times4\times5$	2	50	251	5	6	5.02
	$6\times6\times5$	2	50	260	5	6	5.20
	$12\times12\times5$	2	50	283	5	8	5.66
Beam twist		12.5	8	58	6	8	7.25
Beam bending	$2\times2\times5$	10	10	55	4	10	5.50
	$2\times2\times5$ (a)	10	11	57	4	8	5.18
	$2\times2\times5$ (b)	10	10	53	4	7	5.30
L-shape cantilever		5	20	86	4	5	4.30
Wrenched cantilever	Simultaneous loading	2	59	390	5	11	6.61
	Couple-then-force	2	$50+50$	479	4	8	4.79
45° arc cantilever	$1\times1\times1$	20	5	38	6	10	7.60
	$1\times1\times2$	10	10	65	6	8	6.50
	$1\times1\times4$	10	11	75	5	13	6.82
	$1\times1\times8$	10	12	73	5	8	6.08
	$1\times1\times16$	5	20	118	5	9	5.90

Table 8
Convergence rate of the 45° arc cantilever $1\times1\times2$ from 90% to 100% load

Iteration	Angular-part unknowns		Linear-part unknowns		Biot-axial unknowns	
	Residual norm	Solution norm	Residual norm	Solution norm	Residual norm	Solution norm
1	6.596E+00	1.405E−01	3.000E+01	5.722E+00	6.940E−14	1.468E+03
2	1.554E+04	4.473E−03	2.392E+04	1.086E−01	2.112E−03	8.728E+01
3	6.194E+02	4.133E−03	1.334E+02	1.016E−01	1.197E−05	9.111E+01
4	3.785E+02	2.168E−05	1.099E+02	8.242E−04	8.976E−06	5.982E−01
5	5.264E−02	1.532E−07	8.427E−03	3.903E−06	3.489E−10	1.662E−03
6	2.208E−06	7.116E−14	8.965E−07	2.207E−12	1.549E−13	3.043E−09

number of the tangent matrix increases from 1.E+6 with the self-basing option on, to 1.E+12 with a full pole-based computation, and the total number of iterations rises from 390 to 404.

Table 9
Convergence rate of the wrenched beam from 78% to 80% load

Iteration	Angular-part unknowns			Linear-part unknowns			Biot-axial unknowns		
	Residual norm		Solution norm	Residual norm	Solution norm		Residual norm		Solution norm
	Self-based	Pole-based			Self-based	Pole-based	Self-based	Pole-based	
1	2.546E−01	2.560E−01	6.777E−01	1.273E−02	3.074E+00	2.950E+00	1.476E−15	1.618E−15	2.553E+00
2	4.711E−01	1.190E+01	2.929E−02	2.677E+00	1.187E−01	2.069E−01	6.865E−03		3.718E−01
3	3.847E−02	1.424E−01	9.374E−03	2.868E−02	7.413E−02	9.503E−02	2.776E−05		1.615E−01
4	8.672E−04	4.034E−02	1.033E−04	8.069E−03	3.759E−04	4.425E−04	5.402E−06		6.332E−04
5	3.373E−07	1.262E−06	1.067E−07	4.127E−07	4.708E−07	4.656E−07	1.786E−10		5.925E−07

Comparison with the pole-based analysis.

7. Examples with nearly incompressible elastic material

The next examples concern large strain problems of three-dimensional specimens of rubber-like material. We use a hyperelastic nonlinear constitutive law derived from a well-known Neo-Hookean strain-energy function: $w(\boldsymbol{C}) = \frac{1}{2}\lambda(\ln J)^2 - \mu \ln J + \frac{1}{2}\mu \operatorname{tr}(\boldsymbol{C} - \boldsymbol{I})$, where $\boldsymbol{C} = \boldsymbol{F}^{\mathrm{T}}\boldsymbol{F}$ and $J = \sqrt{\det \boldsymbol{C}}$ (see e.g. Belytschko et al., 2000). In order to fit the constitutive characterization of the non-polar medium, the hyperelastic law must be recast in terms of Biot-type parameters. By understanding the polar decomposition of the deformation gradient $\boldsymbol{F}$ and introducing the right stretch tensor $\boldsymbol{U} = \boldsymbol{I} + \boldsymbol{\varepsilon}^{\mathrm{S}}$, we write as follows the strain-energy function $w(\boldsymbol{U})$ and its derivatives that define the constitutive equation $\hat{\boldsymbol{T}}^{\mathrm{S}} = w_{/\boldsymbol{U}}$ and its tangent map, $\mathbb{E}_{\boldsymbol{\varepsilon}^{\mathrm{S}}\boldsymbol{\varepsilon}^{\mathrm{S}}} = w_{/\boldsymbol{U}\boldsymbol{U}}$:

$$
\begin{aligned}
w(\boldsymbol{U}) &= \frac{1}{2}\hat{\lambda}(\ln\det\boldsymbol{U})^2 - \hat{\mu}\ln\det\boldsymbol{U} + \frac{1}{2}\hat{\mu}\operatorname{tr}(\boldsymbol{U}^2 - \boldsymbol{I}),\\
w_{/\boldsymbol{U}} &= (\hat{\lambda}\ln\det\boldsymbol{U} - \hat{\mu})\boldsymbol{U}^{-1} + \hat{\mu}\boldsymbol{U},\\
w_{/\boldsymbol{U}\boldsymbol{U}} &= \hat{\lambda}\boldsymbol{U}^{-1}\otimes\boldsymbol{U}^{-1} - (\hat{\lambda}\ln\det\boldsymbol{U} - \hat{\mu})(\boldsymbol{U}^{-1}\otimes\boldsymbol{U}^{-1})^{\mathrm{T1423\ S2134\ S1243}} + \frac{1}{2}\hat{\mu}(\mathbb{I} + \breve{\mathbb{I}}).
\end{aligned}
\tag{32}
$$

Here, $\mathbb{I} = \boldsymbol{g}_j\otimes\boldsymbol{g}_k\otimes\boldsymbol{g}^j\otimes\boldsymbol{g}^k$ and $\breve{\mathbb{I}} = \boldsymbol{g}_j\otimes\boldsymbol{g}_k\otimes\boldsymbol{g}^k\otimes\boldsymbol{g}^j$ are fourth-order unitary tensors, and the transpose and symmetry operators are defined so that $(\,)^{\mathrm{T1423}} = (\,)_{ijkl}\ \boldsymbol{g}^i\otimes\boldsymbol{g}^l\otimes\boldsymbol{g}^j\otimes\boldsymbol{g}^k$, $(\,)^{\mathrm{S2134}} = \frac{1}{2}(\,)_{ijkl}(\boldsymbol{g}^i\otimes\boldsymbol{g}^j + \boldsymbol{g}^j\otimes\boldsymbol{g}^i)\otimes\boldsymbol{g}^k\otimes\boldsymbol{g}^l$, $(\,)^{\mathrm{S1243}} = \frac{1}{2}(\,)_{ijkl}\ \boldsymbol{g}^i\otimes\boldsymbol{g}^j\otimes(\boldsymbol{g}^k\otimes\boldsymbol{g}^l + \boldsymbol{g}^l\otimes\boldsymbol{g}^k)$. In Eqs. (32), $\hat{\lambda}$ and $\hat{\mu}$ are the Lamé moduli of the linearized theory. In fact, it can be easily verified that, by evaluating the strain-energy function in the neighborhood of the undeformed configuration $\boldsymbol{U} = \boldsymbol{I}$ via a truncated Taylor expansion of Eq. $(32)_1$, one correctly obtains the quadratic function proper of the linearized theory, Eq. (31).

In this section, we present two geometric/material nonlinear test cases, relating to a cubic body and to a cylindrical shell, respectively, with elastic properties $\hat{\lambda}$ and $\hat{\mu}$ at the limit of compressibility. In such extreme conditions, the present low-order version of the helicoidal element undergoes volumetric locking; so, in order to be able to develop the high deformations of next examples, we resort to the very trivial expedient of a partially reduced integration. This unavoidably deteriorates the precision of the computations, so the quantitative results we present may be unsatisfactory. It is clear that the aim of the following examples is chiefly to show the capability of the element of representing high geometric deformations in a qualitatively acceptable elastic context.

7.1. Compression block

A cube of size $2\times2\times2$ is pinched at two opposite faces by surface loads on the central square area of size 1×1. The elastic properties are $\hat{\lambda} = 400889.806$ and $\hat{\mu} = 80.194$ (which correspond to $\nu = 0.4999$). Due

to symmetry, only an eighth of the block is modeled. The 1/8 model made of $4\times4\times4$ elements and the reference frame placed at the center of the block are shown in Fig. 16. The top surface is constrained in the X and Y directions and the load p is applied as a force per unit surface in the Z direction over 4 surface elements. In the present form, this test case was analyzed by Reese et al. (2000) using special enhanced-strain elements based on an original stabilization technique. In the present computation, we exploit a partially reduced integration, resorting to the full constitutive law from Eqs. (32) at a single, central Gauss point, and to a constitutive law lacking of terms with $\hat{\lambda}$ at the remaining points of the $3\times3\times3$ Gauss quadrature. At load $p=320$, the top mid-point $(0,0,1)$ lowers to $Z=0.410$; this configuration is shown in Fig. 16 along with a graphical representation of the forces applied at the integration points of the surface elements. A considerable compression is observed, however the elements of the top layer suffer from a high distortion that somewhat limits their crushing; so, our model appears much harder than the models of Reese et al. (2000), whose top mid-point is capable of lowering to about $Z=0.305$.

Next, we analyze the same block under a perhaps more natural set of loads and constraints. The top surface is left free in all directions and the load is applied at the surface elements as a pressure that remains normal to the deformed boundary (follower load). As in the previous case, the elements are subjected to a high deformation, but they are much less distorted and the analysis can easily reach the pressure $p=400$. The deformed shapes obtained with three different meshes are depicted in Fig. 17: the imprint profile improves with mesh refinement, while the displacement of the top mid-point $(0,0,1)$ is not much affected, see Fig. 18.

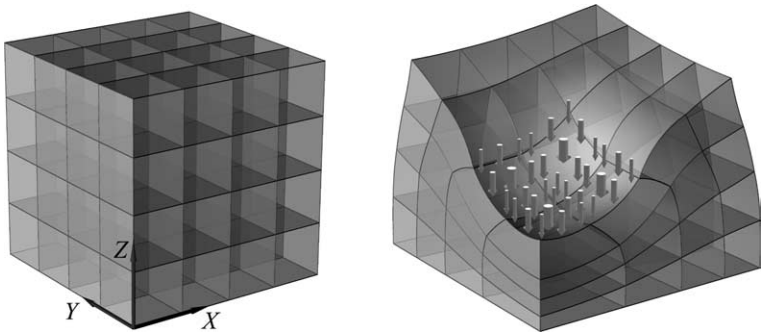

Fig. 16. Compression block. Case of the top surface constrained in the X and Y directions. Undeformed and deformed configuration at dead load $p=320$.

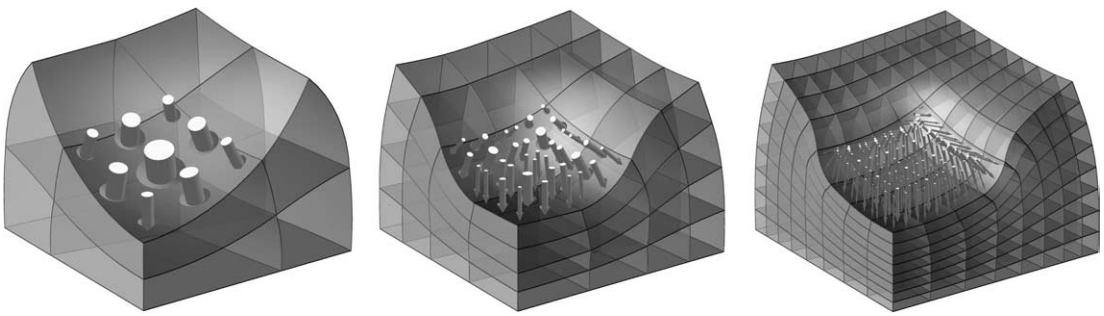

Fig. 17. Compression block. Case of top surface free. Deformed configurations at pressure $p=400$ with three different meshes.

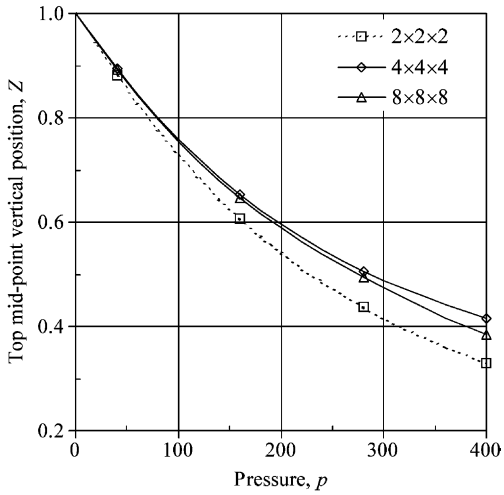

Fig. 18. Compression block. Case of top surface free. Position of the top mid-point versus the pressure load.

7.2. Cylindrical shell

A cylindrical shell of mean radius $R = 9$, length $L = 30$, thickness $t = 2$, is supported along a generatrix and pinched by a radial load along the opposite generatrix. A quarter shell is modeled with a coarse mesh of $4 \times 8 \times 2$ elements, see Fig. 19; the load is applied as a distributed force on eight surface elements on the upper longitudinal section, and the ground support is placed at the outer line of nodes. Two sets of material properties are considered: (a) $\hat{\lambda} = 24,000$, $\hat{\mu} = 6000$ (i.e. $v = 0.4$), and (b) $\hat{\lambda} = 240,000$, $\hat{\mu} = 6000$ (i.e. $v = 0.4878$). The shell of material (a) is analyzed using either a full quadrature on 27 Gauss points per element, or a partially reduced integration with modulus $\hat{\lambda}$ contributing only at the central Gauss point. The latter integration only is used with the nearly incompressible material (b). Due to the reduced integration, two elements must be used across the thickness to capture bending. The load-deflection plots of three

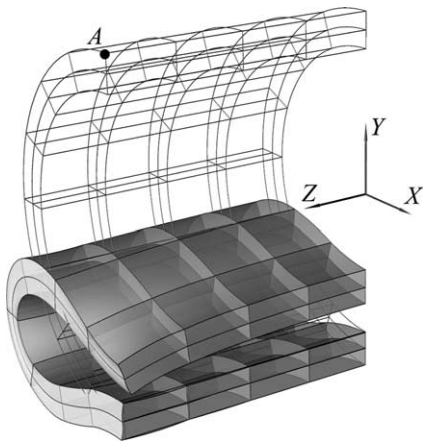

Fig. 19. Cylindrical shell. Deformed configuration of model with material (b) and partially reduced integration under force per unit length $f = 500$.

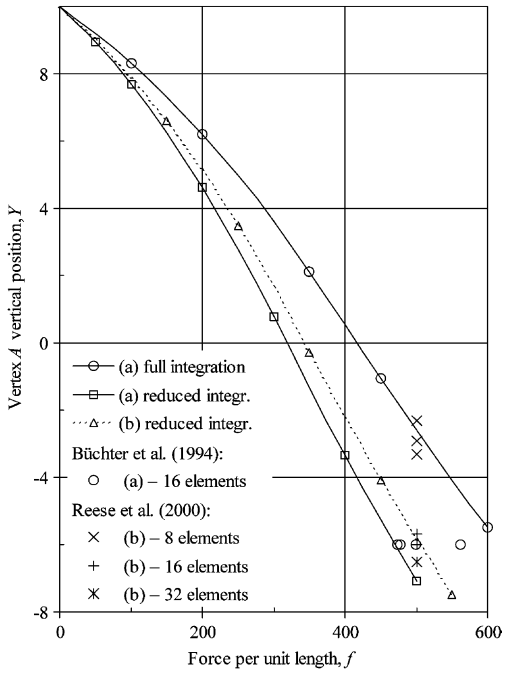

Fig. 20. Cylindrical shell. Position of vertex A versus the pinching load in three analyses with materials (a) and (b). Comparison with published results with different formulations and number of elements in circumferential direction.

analyses are shown in Fig. 20, where they can be compared with the results from Büchter et al. (1994) for material (a), and from Reese et al. (2000) for material (b). The results from the quoted papers were obtained by means of stabilized enhanced-strain three-dimensional elements (using a single element across the thickness), or by means of accurate shell elements. So, we do not pretend to compete in precision with such results, using the modest expedient of a partially reduced integration. Instead, our purpose here is to show the suitability of the helicoidal element in the geometric modeling of high deformations of relatively thin bodies: this goal seems to be achieved, as evidenced by the deformed shape in Fig. 19, which is very close to that published by Reese et al. (2000).

8. An example of linear analysis

We conclude our papers with a brief excursus in linear analysis, in the attempt to explain the significance of linear elasticity in a helicoidal modeling context. As customarily understood, a linear elastic finite element computation is performed in a single step with a coefficient matrix built on the reference configuration; then, the solution is used to update the model status according to the underlying modeling of the continuum. In a plain Euclidean context, this simply means taking the kinematical solution as the displacements of the model nodes. In the helicoidal modeling, instead, the kinematical solution represents the helices of the rototranslations of the nodal frames, and consistently the model status must be updated multiplicatively also in a linear analysis. Therefore, when adhering to the helicoidal modeling, in a linear analysis the displacements are not expected to be proportional to loads. Note that the situation is analogous to the simple 1-d.o.f. planar problem of a rigid body loaded by a couple and restrained by a torsional spring of constant stiffness.

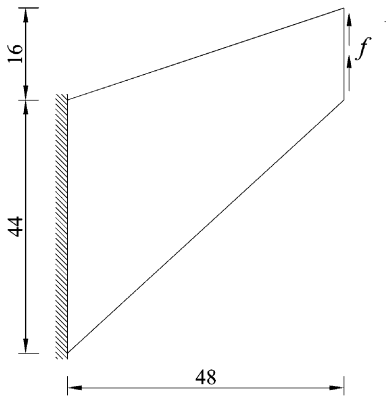

Fig. 21. Linear example. Cook's membrane data.

In order to evaluate the performance of the helicoidal modeling in linear elasticity, let us examine a classical plane stress case, the Cook membrane (Fig. 21) with data from Simo et al. (1989): elastic properties $E = 1$, $v = 0.33$, and tip force $F = 1$ (i.e. $f = 1/16$). The planar model consists of a regular mesh of 8×8 trapezoidal elements and is loaded at 8 straight tip elements. Three kinds of computations are compared: (i) a full *nonlinear* analysis, which for our present purpose can be regarded as the reference (exact) solution; (ii) a series of distinct linear analyses performed in a single step from the undeformed mesh under increasing load values, and exploiting the consistent updating of the status as proposed above; and (iii) another series of distinct linear analyses that use, instead, the classical additive updating of the position field and the multiplicative updating of the orientation field. (Note that in the last computation, the geometric stiffness due to target load, Eq. $(24)_2$, has been zeroed, so as to match as closely as possible the classical concept of a purely elastic stiffness matrix.) We refer to cases (ii) and (iii) as the *helicoidal* linear solution and the *Euclidean* linear solution, respectively. Both are linear analyses, but in the *helicoidal* solution we are updating in a multiplicative manner the oriento-position field as a whole, made of a linear part and an angular part that are intimately coupled, while in the *Euclidean* solution we are updating separately the position and the orientation fields.

The *helicoidal* and the *Euclidean* linear computations are compared to the *nonlinear* analysis in the left and right sketches of Fig. 22, respectively. The *helicoidal* solution is quite close to the *nonlinear* solution at least up to the 50% load, when the response can hardly be said to be infinitesimal; the *Euclidean* solution, instead, departs from the exact solution earlier. It is also worth noting that the displacement in the Y direction is not proportional to the load in the *helicoidal* linear solution, while it is by construction in the *Euclidean* linear solution. In Fig. 23, the plots of the tip force versus the vertical displacement of the tip mid point are compared: the *nonlinear* and the *helicoidal* linear solutions match remarkably, while of course, only the *Euclidean* linear solution permits a comparison with the results from literature for linear elasticity from a Euclidean standpoint.

The convergence of the helicoidal element in linear plane stress has been attested by analyzing a family of six meshes generated by bisection, ranging from 1×1 to 32×32, and comparing the positions reached by point B on the plane of the membrane at a relatively small load ($F = 0.1$). The *helicoidal* linear solution does converge, as can be seen graphically in Fig. 24, where the target *nonlinear* solution is also shown.

The results of the present example bring out two interesting features of a finite element analysis under the helicoidal modeling. First, it can be seen in Fig. 22(a) that the *helicoidal* linear solution is apparently a fairly good approximation of the reference (*nonlinear*) solution as long as the loads are reasonably low, while at

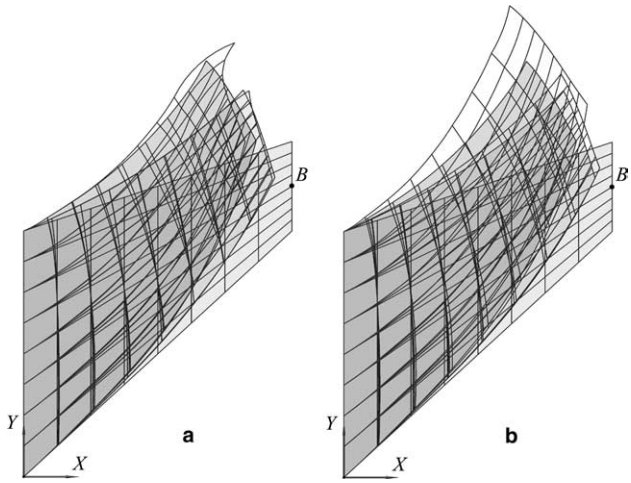

Fig. 22. Linear example. Undeformed model and deformed configurations at 50% and 100% load. Comparison of the *nonlinear* solution (solid) with (a) the *helicoidal* linear solution, and (b) the *Euclidean* linear solution.

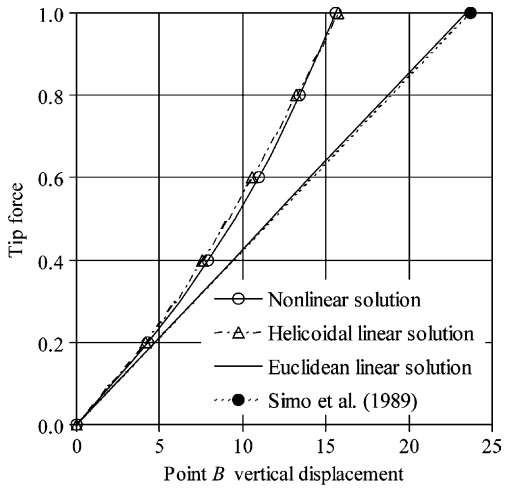

Fig. 23. Linear example. Tip force versus displacement of point B in Y direction.

loads as large as $F = 1$ the deformed shape is manifestly wrong. Second, we saw that the badness of the deformed shape in the upper right corner at 100% load increases hugely with mesh refinement (from mesh 1×1 to mesh 32×32). The *Euclidean* linear solution in Fig. 22 (b) does not show a similar behavior, so these features are likely to be peculiar to the helicoidal updating process. As a consequence, a helicoidal linear analysis is practicable only up to a relatively small change of configuration, and even more so, the more detailed is the mesh. On the other hand, the *Euclidean* solution is less precise already at low load levels. These considerations also affect the nonlinear analyses, so the small load steps that must be applied during a nonlinear solution process (see Table 7) are less surprising. It must be noted, however, that performing a nonlinear analysis with the uncoupled updating of the position and the orientation fields, as in the *Euclidean* solution, almost doubles the total number of iterations.

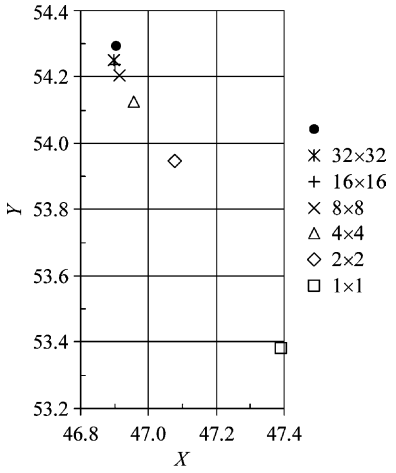

Fig. 24. Linear example. Positions of point B at 10% load after *helicoidal* linear solution using six different meshes. The reference solution (mesh 32×32) is marked with a bullet.

9. Conclusion

In the present Part III, the helicoidal modeling has been applied to finite elasticity analyses of simple materials unable of carrying couple-stresses. Thanks to a straightforward constitutive characterization, it was possible to exploit the sound variational formulation and the relevant consistent linearization developed in Part I for the polar medium. The finite-element approximation of the ensuing variational principle is based on the multiplicative interpolation developed in Part II and results in volume and surface elements having nodal oriento-positions as degrees-of-freedom. To develop successful nonlinear finite elements, several unusual issues had to be overcome: the resolution of the mixed variation variables at the nodal level, the methodology of analysis based on the multiplicative updating of the kinematical unknowns, the interpolation of the Biot-axial field between the element faces. The kinematical interpolation and the analysis methodology ensure frame-invariant and path-independent solutions, as demonstrated in Part II and evidenced in the example of the wrenched cantilever.

The examples discussed above show the ability of the proposed low-order element to model curved bodies and to bend up to near π, even if meshes are coarse or irregular. The element has been tested in high deformation problems with large three-dimensional rotations and shows a remarkable performance in bending-dominated problems. Moreover, a few examples allow to understand that the helicoidal modeling is also practicable when materials are nearly incompressible, and can produce accurate results also in linear elasticity, if a really infinitesimal response is expected. However, the helicoidal element (which actually cannot be said to be a cheap element) is susceptible of being ameliorated, for instance by means of a p-extension, which could allow to elude the volumetric locking occurring at the limit of compressibility. Also the lengthy solution process requiring small load steps is a research topic worthy of further investigation.

As a final comment about the proposed helicoidal modeling, we wish to stress (in addition to a mere theoretical interest) its effectiveness in computational solid mechanics. The Euclidean standpoint leads to the well established classical modeling underlying the most common variational principles in continuum mechanics, even when rotational degrees-of-freedom are accounted for (e.g. Atluri and Cazzani, 1995; Merlini, 1997). However, when approximating for computational purposes a variational principle with rotational unknowns by the finite element method, then it is easy to realize that low-order elements are destined to produce an inconsistent kinematical field over the element domain unless one couples positions and

orientations. A natural coupling of positions and orientations is inherent in the proposed helicoidal modeling. It is worth noting that this coupling would be of significant advantage within a shell theory, as one can guess from the example of the cylindrical shell.

References

Angeles, J., 1998. The application of dual algebra to kinematic analysis. In: Angeles, J., Zakhariev, E. (Eds.), Computational Methods in Mechanical Systems, vol. 161. Springer-Verlag, Heidelberg, pp. 1–31.

Atluri, S.N., 1984. Alternate stress and conjugate strain measures, and mixed variational formulations involving rigid rotations, for computational analyses of finitely deformed solids, with application to plates and shells—I, Theory. Comput. Struct. 18, 93–116.

Atluri, S.N., Cazzani, A., 1995. Rotations in computational solid mechanics. Arch. Comput. Meth. Engng. 2, 49–138.

Bathe, K.-J., Bolourchi, S., 1979. Large displacement analysis of three-dimensional beam structures. Int. J. Numer. Meth. Engng. 14, 961–986.

Belytschko, T., Liu, W.K., Moran, B., 2000. Nonlinear Finite Elements for Continua and Structures. John Wiley & Sons, Chichester, England.

Büchter, N., Ramm, E., Roehl, D., 1994. Three-dimensional extension of non-linear shell formulation based on the enhanced assumed strain concept. Int. J. Numer. Meth. Engng. 37, 2551–2568.

Bufler, H., 1985. The Biot stresses in nonlinear elasticity and the associated generalized variational principles. Ing. Arch. 55, 450–462.

Eringen, A.C., 1966. Linear theory of micropolar elasticity. J. Math. Mech. 15, 909–923.

Felippa, C.A., 1992. Parametrized variational principles for micropolar elasticity. Int. J. Solids Struct. 29, 2709–2721.

Fraeijs de Veubeke, F.B., 1972. A new variational principle for finite elastic displacements. Int. J. Engng. Sci. 10, 745–763.

Hughes, T.J.R., 1987. The Finite Element Method—Linear Static and Dynamic Finite Element Analysis. Prentice-Hall, Inc., Eglewood Cliffs, New Jersey.

Hughes, T.J.R., Brezzi, F., 1989. On drilling degrees of freedom. Comput. Meth. Appl. Mech. Engng. 72, 105–121.

Ibrahimbegović, A., Frey, F., 1993. Geometrically non-linear method of incompatible modes in application to finite elasticity with independent rotations. Int. J. Numer. Meth. Engng. 36, 4185–4200.

Ibrahimbegović, A., Frey, F., 1995. Variational principles and membrane finite elements with drilling rotations for geometrically nonlinear elasticity. Int. J. Numer. Meth. Engng. 38, 1885–1900.

Klinkel, S., Wagner, W., 1997. A geometrical non-linear brick element based on the EAS-method. Int. J. Numer. Meth. Engng. 40, 4529–4545.

Kožar, I., Ibrahimbegović, A., 1995. Finite element formulation of the finite rotation solid element. Finite Elements Anal. Des. 20, 101–126.

Merlini, T., 1997. A variational formulation for finite elasticity with independent rotation and Biot-axial fields. Comput. Mech. 19, 153–168.

Merlini, T., Morandini, M., 2002. Variational formulations for helicoidal modeling in finite elasticity. DIA-SR 02-17, Dip. Ing. Aerospaziale, Politecnico di Milano.

Merlini, T., Morandini, M., 2004a. On the modeling of elastic solids by using orthonormal dual tensors. Mater. Phys. Mech. 7, 45–53.

Merlini, T., Morandini, M., 2004b. Finite elements for helicoidal modeling in finite elasticity. DIA-SR 04-12, Dip. Ing. Aerospaziale, Politecnico di Milano.

Merlini, T., Morandini, M., 2004c. The helicoidal modeling in computational finite elasticity. Part I: Variational formulation. Int. J. Solids Struct. 41, 5351–5381.

Merlini, T., Morandini, M., 2004d. The helicoidal modeling in computational finite elasticity. Part II: Multiplicative interpolation. Int. J. Solids Struct. 41, 5383–5409 (Also: Erratum, Int. J. Solids Struct. 42, 1269).

Moita, G.F., Crisfield, M.A., 1996. A finite element formulation for 3-D continua using the co-rotational technique. Int. J. Numer. Meth. Engng. 39, 3775–3792.

Reese, S., Wriggers, P., Reddy, B.D., 2000. A new locking-free brick element technique for large deformation problems in elasticity. Comput. Struct. 75, 291–304.

Reissner, E., 1965. A note on variational principles in elasticity. Int. J. Solids Struct. 1, 93–95.

Reissner, E., 1984. Formulation of variational theorems in geometrically nonlinear elasticity. J. Engng. Mech. 110, 1377–1390.

Ritto-Corrêa, M., Camotim, D., 2002. On the differentiation of the Rodrigues formula and its significance for the vector-like parameterization of Reissner–Simo beam theory. Int. J. Numer. Meth. Engng. 55, 1005–1032.

Roark, R.J., Young, W.C., 1975. Formulas for Stress and Strain, fifth ed. McGraw Hill, Tokyo.

Seki, W., Atluri, S.N., 1994. Analysis of strain localization in strain-softening hyperelastic materials, using assumed stress hybrid elements. Comput. Mech. 14, 549–585.

Seki, W., Atluri, S.N., 1995. On newly developed assumed stress finite element formulations for geometrically and materially nonlinear problems. Finite Elements Anal. Des. 21, 75–110.

Simo, J.C., Fox, D.D., Rifai, M.S., 1989. On a stress resultant geometrically exact shell model. Part II: The linear theory; computational aspects. Comput. Meth. Appl. Mech. Engng. 73, 53–92.

Simo, J.C., Fox, D.D., Hughes, T.J.R., 1992. Formulation of finite elasticity with independent rotations. Comput. Meth. Appl. Mech. Engng. 95, 277–288.

Wisniewski, K., 1998. A shell theory with independent rotations for relaxed Biot stress and right stretch strain. Comput. Mech. 21, 101–122.

Yeh, J.-T., Chen, W.-H., 1993. Shell elements with drilling degree of freedoms based on micropolar elasticity theory. Int. J. Numer. Meth. Engng. 36, 1145–1159.

Zupan, D., Saje, M., 2003. Finite-element formulation of geometrically exact three-dimensional beam theories based on interpolation of strain measures. Comput. Meth. Appl. Mech. Engng. 192, 5209–5248.